

---

# **A Correlation Between Flight-Determined Derivatives and Wind-Tunnel Data for the X-24B Research Aircraft**

---

Alex G. Sim

---

August 1997



National Aeronautics and  
Space Administration

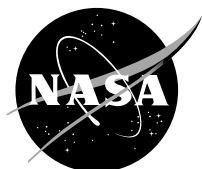
---

# A Correlation Between Flight-Determined Derivatives and Wind-Tunnel Data for the X-24B Research Aircraft

---

Alex G. Sim  
*NASA Dryden Flight Research Center  
Edwards, California*

1997



National Aeronautics and  
Space Administration

Dryden Flight Research Center  
Edwards, California 93523-0273

## INTRODUCTION

The X-24B research aircraft is one of a series of vehicles with a geometric shape that permits both entry to the earth's atmosphere and horizontal landing. Prior vehicle shapes intended for this purpose include those of the M-2, HL-10, and X-24A research aircraft. The design of those vehicles, called lifting bodies, was conceptually constrained by the level of high temperature material technology, which dictated a blunt, wingless shape. However, recent advances in high temperature materials allowed the X-24B aircraft to be designed with a highly swept delta wing, which permits more efficient hypersonic cruise. Much of the X-24B research aircraft was constructed by using the hardware and structure of the X-24A research vehicle.

The X-24B vehicle was flight tested in a research program that was conducted jointly by the National Aeronautics and Space Administration (NASA) and the United States Air Force. During the envelope expansion part of the flight program, flight derivatives were acquired to update the flight simulator, which was used for flight planning, pilot training, and handling qualities and control system studies, and to update the analysis of the vehicle dynamics and handling qualities to insure safety of flight. Furthermore, by correlating the flight derivatives with wind-tunnel predictions, another program goal was attained—the provision of a data base with which experimental and analytical prediction techniques for this class of aircraft could be improved.

This report presents the correlation between the flight-determined derivatives and wind-tunnel predictions for the first 21 flights of the X-24B research aircraft. The flight derivatives were obtained with a modified maximum likelihood estimation method used at the NASA Flight Research Center. Previous experience with this estimation method for related configurations is discussed in references 1 and 2.

## SYMBOLS

Derivatives are presented as standard NASA coefficients of forces and moments. A right-hand sign convention is used to determine the direction of forces, moments, angular displacements, and velocity. Data are referenced to the vehicle body axes.

Physical quantities are given in the International System of Units (SI) and parenthetically in U.S. Customary Units. All measurements were taken in U.S. Customary Units.

$b$	reference airplane span, m (ft)
$\bar{c}$	reference aircraft length, m (ft)
$I_X$	rolling moment of inertia, kg-m <sup>2</sup> (slug-ft <sup>2</sup> )
$I_{XZ}$	product of inertia, kg-m <sup>2</sup> (slug-ft <sup>2</sup> )
$I_Y$	pitching moment of inertia, kg-m <sup>2</sup> (slug-ft <sup>2</sup> )
$I_Z$	yawing moment of inertia, kg-m <sup>2</sup> (slug-ft <sup>2</sup> )
$M$	Mach number
$p$	rolling rate, deg/sec
$q$	pitching rate, deg/sec

$r$	yawing rate, deg/sec
$V$	velocity, m/sec (ft/sec)
$\alpha$	angle of attack, deg
$\beta$	angle of sideslip, deg
$\delta_a$	aileron deflection, $(\delta_{a_{left}} - \delta_{a_{right}})$ , deg
$\delta_{a_b}$	aileron bias deflection, $1/2 (\delta_{a_{left}} + \delta_{a_{right}})$ , deg
$\delta_e$	lower-flap deflection, $1/2 (\delta_{e_{left}} + \delta_{e_{right}})$ , deg
$\delta_r$	upper-rudder deflection, $1/2 (\delta_{r_{left}} + \delta_{r_{right}})$ , deg
$\delta_{r_b}$	rudder-bias deflection, $1/4 (\delta_{r_{left}} - \delta_{r_{right}} + \delta_{r_{L_{left}}} - \delta_{r_{L_{right}}})$ , deg
$\delta_{r_L}$	lower-rudder deflection, deg
$\delta_u$	upper-flap deflection, $1/2 (\delta_{u_{left}} + \delta_{u_{right}})$ , deg
$\delta_{u_b}$	upper-flap bias, $1/2 (\delta_{u_{left}} + \delta_{u_{right}})$ , deg
$C_l$	rolling-moment coefficient
$C_m$	pitching-moment coefficient
$C_N$	normal force coefficient
$C_n$	yawing-moment coefficient
$C_Y$	side-force coefficient

Nondimensional derivatives, where  $i = \alpha, \delta_e; j = \beta, \delta_r, \delta_a$ ; and  $k = p, r$ :

Longitudinal -

$$C_{m_i} = \frac{\partial C_m}{\partial i}$$

$$C_{N_i} = \frac{\partial C_N}{\partial i}$$

$$C_{m_q} = \frac{\partial C_m}{\partial \frac{q\bar{c}}{2V}}$$

Lateral-directional -

$$C_{l_j} = \frac{\partial C_l}{\partial j}$$

$$C_{n_j} = \frac{\partial C_n}{\partial j}$$

$$C_{Y_j} = \frac{\partial C_Y}{\partial j}$$

$$C_{l_k} = \frac{\partial C_l}{\partial \frac{kb}{2V}}$$

$$C_{n_k} = \frac{\partial C_n}{\partial \frac{kb}{2V}}$$

## **X-24B RESEARCH AIRCRAFT**

The X-24B research aircraft (fig. 1) has a highly swept delta planform with three vertical fins and a boattailed afterbody. Combinations of the four chambers of the XLR11 rocket engine are used in powered flight. Aircraft dimensions are shown in figure 2, and aircraft physical characteristics are given in table 1. Typical variations of the moments of inertia and center of gravity with changes in gross weight are presented in table 2.

### **Flight Control System**

The primary manual control system was an irreversible hydraulic system. The pilot controlled the aircraft through a conventional center stick and rudder pedals. The primary aircraft control surface movements, which were activated by both pilot inputs and the stability augmentation system, were symmetric deflection of the two lower flaps for pitch, differential deflection of the strake ailerons for roll, and deflection of the upper rudders for yaw. The control surface locations and sign convention are shown in figure 3.

The primary stability augmentation system was a three-axis rate feedback system. An interconnect provided a rudder control input in addition to an aileron control input for a pilot-commanded aileron input. The rate feedback and interconnect gains could be adjusted by the pilot in flight. The pilot could also select an automatic mode for the interconnect gain; in the automatic mode, the gain was varied as a function of angle of attack.

### **Aircraft Configuration**

Two aircraft configurations were used to obtain the data presented in this report. A subsonic configuration was used to achieve good aerodynamic performance with adequate stability at subsonic speeds, and a transonic configuration was used to achieve good stability at transonic and supersonic speeds. In the subsonic configuration, the upper flaps were biased 20° above the upper surface of the body (i.e.,  $\delta_{u_b} = -20^\circ$ ), and the rudders were biased (toed in) 10° (i.e.,  $\delta_{r_b} = -10^\circ$ ). In the transonic configuration,  $\delta_{u_b} = -40^\circ$  and  $\delta_{r_b} = 0^\circ$ . In both configurations, both ailerons were biased down 7° (i.e.,  $\delta_{a_b} = 7^\circ$ ), which increased the camber of the strakes.

## INSTRUMENTATION

Data were obtained by means of a 9-bit pulse code modulation telemetry system and were analyzed by using a ground-based computer.

Angle of attack and angle of sideslip were measured by using an instrumented NACA nose boom (ref. 3). Angular positions were measured by using a stable platform; angular rates were measured by using rate gyros; and linear accelerations were measured by using conventional accelerometers. Control surface positions were measured by using control position transducers.

Corrections were applied to angle of attack and angle of sideslip data for angular rates and boom bending. Upwash corrections were found to be negligible in windtunnel tests and were therefore ignored. Velocity, altitude, and Mach number were calculated on the basis of corrected dynamic and static pressures. Linear accelerations were corrected for displacement from the center of gravity. Previous error analyses of NASA Flight Research Center instrumentation systems have shown the instrumentation errors to be negligible for derivative extraction.

## FLIGHT TESTS

Weight and balance measurements were made as needed to verify the location of the aircraft's center of gravity, which varied from  $0.65\bar{c}$  to  $0.66\bar{c}$ . Moments of inertia were determined experimentally before the first flight by means of an inertia swing technique. Flight values for the inertial were calculated based on the current aircraft changes and propellant utilization.

The X-24B aircraft was air launched from a modified B-52 airplane at an altitude of approximately 13,700 meters (45,000 feet) and a Mach number of approximately 0.7. After launch, the pilot flew a planned flight profile. The unpowered flights lasted approximately 4 minutes and were conducted below a Mach number of 0.7. For the powered flights, the rocket engine was fired approximately 5 seconds after launch and was operated for approximately 130 seconds. The powered boost was followed by gliding flight. The entire flight lasted approximately 7 minutes. For both types of flights, an angle of attack schedule was flown to achieve the desired flight profile and flight conditions for the planned data maneuvers.

In general, the maneuvers from which vehicle data were obtained were performed at altitudes above approximately 6100 meters (20,000 feet) to allow the pilot enough time to prepare for the final approach and landing. The trajectories flown precluded steady flight conditions. The vehicle's stability augmentation system was generally engaged while stability and control maneuvers were performed.

Because of the short time available for obtaining flight data and the rapid changes in the flight conditions, there was only one opportunity to perform each maneuver per flight. Therefore, maneuvers were practiced on a simulator before each flight. The longitudinal maneuver was a pulse or doublet of the lower flaps followed by 2 seconds to 5 seconds without pilot input. The lateral-directional maneuver was a rudder doublet followed by 2 seconds to 5 seconds without pilot input and then an aileron doublet. Data were obtained over a Mach number range from 0.35 to 1.72 and over an angle of attack range from  $3.5^\circ$  to  $15.7^\circ$ .

## METHOD OF ANALYSIS

A digital computer program that employed a maximum likelihood estimation method was used to determine sets of derivatives in either the longitudinal or lateral-directional mode from the flight data. The computer program and its use, theory, and mathematical model are documented in references 4 and 5.

## WIND-TUNNEL DATA

The predictions used in this report are based on wind-tunnel data obtained from four wind-tunnel test facilities. Most of the power-off data were acquired during a study conducted in the Cornell Aeronautical Laboratory (now Calspan) 8-Foot Transonic Wind Tunnel; these data are for Mach numbers of 0.4, 0.6, 0.7, 0.8, 0.9, 0.95, 1.0, 1.15, and 1.3. The power-off data obtained at Mach numbers of 1.5 and 1.72 were obtained at the Arnold Engineering Development Center von Kármán Gas Dynamics Facility Supersonic Wind Tunnel A (refs. 6 and 7). The power-on increments for Mach numbers of 0.6, 0.8, 0.9, 0.95, and 1.2, as well as limited power-off data at Mach numbers of 0.6, 0.7, and 0.8, were obtained in the Langley 16-Foot Transonic Tunnel. To show the effects of the gear, limited data were obtained at the Air Force Institute of Technology 5-Foot Subsonic Wind Tunnel for a Mach number of 0.17 with the gear both up and down (ref. 8).

To account properly for the effects of rocket power on the vehicle's aerodynamics in wind-tunnel testing, both the rocket's momentum flux ratio and pressure ratio should be duplicated. However, this is not physically possible in a scaled model test. To approximate the effects of power on the X-24B derivatives, two sets of windtunnel tests were conducted, first with the momentum flux ratio scaled properly and then with the pressure ratio scaled properly. The maximum incremental changes in the derivatives due to power from these two sets of wind-tunnel tests were added to the best power-off predictions to indicate the trend due to power. As a result, the power-on data should be used to indicate trends and not actual values. Since power-on data were not obtained at Mach numbers greater than 1.2, the increments for a Mach number of 1.2 were applied to all data above this Mach number. This procedure further degraded the power-on wind-tunnel predictions.

All predicted damping derivatives were estimated as a function of Mach number before the first flight. The total damping derivatives are represented in this report by their rotary derivative counterparts.

## DATA PRESENTATION AND DISCUSSION

Most of the following discussion concerns differences between flight and predicted results. Derivatives that do not greatly affect the aircraft's response are not discussed in detail. Furthermore, not all derivatives were obtained from each maneuver, and some that were obtained were considered invalid and are therefore not presented. On the whole, the consistency of the flight derivatives and their correlation with the wind-tunnel predictions were better than expected based on past experience. The flight derivatives, which were obtained by using a modified maximum likelihood estimation method, provided good documentation of the aircraft's characteristics.

Uncertainty levels were obtained at the same time as the flight derivatives in the computer program analysis. These uncertainty levels are a measure of the amount of information provided by a maneuver for each derivative. For most maneuvers analyzed, they can also be interpreted as a measure of the accuracy

of the derivative value. Usually, if the magnitude of the uncertainty level is large, the accuracy of the derivative value is poor. However, the converse is not necessarily true. In the figures, uncertainty levels are shown only if their boundaries are outside the space occupied by the symbol that represents the derivative.

## Longitudinal Derivatives

Flight and wind-tunnel longitudinal derivatives are compared in figures 4 to 10 for Mach numbers from 0.4 to 1.5. The effects of configuration changes are shown in figures 4 and 5; the effects of power are shown in figures 5, 6, 8, 9, and 10.

In the Mach number range from 0.47 to 0.92 (figs. 4 to 6), the longitudinal static stability parameter,  $C_{m_\alpha}$ , is smaller than predicted and the primary longitudinal control effectiveness parameter,  $C_{m_{\delta_e}}$ , is the same as or slightly greater than predicted. The longitudinal damping parameter,  $C_{m_q}$ , is generally lower than estimated in the subsonic configuration (fig. 4). For the transonic configuration, however,  $C_{m_q}$  is near predictions for Mach numbers less than 0.75 (fig. 5) and usually greater than estimated at Mach numbers between 0.75 and 0.92 (fig. 6). The flight-determined coefficient of normal force due to angle of attack,  $C_{N_\alpha}$ , should correspond to predictions based on untrimmed longitudinal control settings. However, the flight derivatives are generally below the untrimmed predictions and above the trimmed predictions. The flight-determined coefficient of normal force due to lower flap,  $C_{N_{\delta_e}}$ , agrees reasonably well with the wind-tunnel predictions. No power effects are apparent in the four power-on points in figures 5 and 6.

Only two flight data points were obtained at Mach numbers near 0.95 (fig. 7). They indicate  $C_{m_\alpha}$  to be slightly smaller than predicted and  $C_{m_{\delta_e}}$  to remain greater than predicted. The flight value of  $C_{m_q}$  does not agree with the estimated value. It may not be possible to determine a consistent value for  $C_{m_q}$  in the Mach number range from 0.85 to 1.35, because the normal unsteadiness of the transonic flow is aggravated by regions of separated flow on the aft part of the aircraft. Tuft studies confirmed the existence of the separated flow regions. In addition, the airplane's response is overdamped by the stability augmentation system. The flight values for  $C_{N_\alpha}$  and  $C_{N_{\delta_e}}$  have higher than usual uncertainty levels, but for the transonic region the data are considered to be good.

In the Mach number range between 0.98 and 1.33 (figs. 8 and 9),  $C_{m_\alpha}$  is usually smaller than predicted and  $C_{m_{\delta_e}}$  is slightly greater. The flight values for  $C_{N_\alpha}$  are smaller than the untrimmed predictions, and  $C_{N_{\delta_e}}$  is close to predictions. Smaller power-on values for  $C_{m_\alpha}$  and  $C_{N_\alpha}$  indicate a power effect.



The flight data obtained above a Mach number of 1.33 (fig. 10) indicate  $C_{m_\alpha}$  and  $C_{m_{\delta_e}}$  to be greater than predicted and  $C_{m_q}$  to be lower than predicted. The flight values of  $C_{N_\alpha}$  are lower than the untrimmed predictions, and  $C_{N_{\delta_e}}$  is near the predictions. The effects of power are slight.

Figure 11 summarizes  $C_{m_\alpha}$  and  $C_{m_{\delta_e}}$  for the angle of attack range from  $4^\circ$  to  $12^\circ$ . The data show  $C_{m_\alpha}$  to be generally smaller than predicted and  $C_{m_{\delta_e}}$  to be slightly greater than predicted.

## Lateral-Directional Derivatives

It was predicted that the static stability derivatives,  $C_{l_\beta}$ ,  $C_{n_\beta}$ , and  $C_{Y_\beta}$ , and the rudder derivatives,  $C_{l_{\delta_r}}$ ,  $C_{n_{\delta_r}}$ , and  $C_{Y_{\delta_r}}$ , would be affected by airplane configuration, so the derivatives for the two aircraft configurations are presented separately in figure 12. The aileron derivatives,  $C_{l_{\delta_a}}$ ,  $C_{n_{\delta_a}}$ , and  $C_{Y_{\delta_a}}$ , were neither predicted nor found to be configuration sensitive. The damping derivatives,  $C_{l_p}$ ,  $C_{n_p}$ ,  $C_{l_r}$ , and  $C_{n_r}$ , were not found to be configuration sensitive. Therefore the aileron and damping derivatives for both configurations are shown in the same plots in figure 12.

As shown by figures 12(a) and 12(b),  $C_{n_\beta}$  is usually greater than predicted at Mach numbers less than approximately 0.7. In figures 12(c), 12(d), and 12(e), the primary control derivatives,  $C_{n_{\delta_r}}$  and  $C_{l_{\delta_a}}$ , are at the same level or greater than predicted, and  $C_{n_{\delta_a}}$  is at the same level or smaller than predicted. In figure 12(f),  $C_{l_p}$  is higher than estimated and  $C_{n_p}$  is less positive than estimated. Good flight estimates of  $C_{l_r}$  and  $C_{n_r}$  were not obtained because only small yaw rates were generated.

Predictions indicated that power affected  $C_{l_\beta}$  and  $C_{n_\beta}$  at or above a Mach number of 0.8. A power effect was also predicted for  $C_{Y_\beta}$  above a Mach number of 0.95. To show the power-on predictions for these derivatives, a separate plot is used for each wind-tunnel Mach number in figures 13 to 16. It should be remembered that the power-on predictions are based on the maximum wind-tunnel power-on increment and that the trends rather than the values of the data should be considered. The other derivatives were less sensitive to Mach number and power, and therefore data for ranges of Mach numbers are plotted together.

For two reasons, the Mach number region from 0.8 to 1.0 (fig. 13) is the most difficult in which to obtain consistent results. First, aerodynamic nonlinearities occur because of the complex nature of the transonic flow. The uncertainty levels in this region are often large, particularly at high angles of attack,

which indicates that the estimates of the flight derivatives are poor. Second, the sensitivity of the derivatives to Mach number is greatest between Mach numbers of 0.9 and 1.0. Because of this, small variations in Mach number cause scatter in the data. This is also a problem in other Mach number ranges, but to a lesser extent.

The static stability derivatives obtained near Mach numbers of 0.8, 0.9, and 0.95 (fig. 13(a)) indicate a reduction in static stability due to the effects of power and angle of attack near a Mach number of 0.95. Figure 13(b) indicates that  $C_{n_{\delta_r}}$  was greater than predicted. Results from figures 13(b) and 13(c) indicate that  $C_{l_{\delta_r}}$  and  $C_{l_{\delta_a}}$  were the same as predicted, but that  $C_{n_{\delta_a}}$  was smaller. In figure 13(d),  $C_{l_p}$  was the same as estimated.

Derivatives obtained near Mach numbers of 1.0, 1.1, and 1.2 are presented in figure 14. The power-off flight values for  $C_{l_\beta}$  and  $C_{n_\beta}$  near a Mach number of 1.0 (fig. 14(a)) are near the predicted values at low angles of attack and greater than predicted at high angles of attack. The flight values of  $C_{l_\beta}$  and  $C_{n_\beta}$  near a Mach number of 1.1 (fig. 14(a)) are near the predictions, and the power-off values of  $C_{l_\beta}$  and  $C_{n_\beta}$  near a Mach number of 1.2 are smaller than predicted. From figure 14(a) it is apparent that the power-on flight data are generally at a lower stability level than the power-off flight data. In figures 14(b) and 14(c),  $C_{l_{\delta_r}}$  and  $C_{n_{\delta_r}}$  are near predictions, whereas  $C_{l_{\delta_a}}$  is greater than predicted. The derivative  $C_{n_{\delta_a}}$  is smaller than predicted at low angles of attack.

The derivatives obtained near Mach numbers of 1.3, 1.4, and 1.5 are presented in figure 15; derivatives obtained near a Mach number of 1.6 are presented in figure 16. Figures 15(a) and 16(a) show that  $C_{l_\beta}$  is reasonably close to predictions; therefore, changes in static stability are attributed to changes in  $C_{n_\beta}$ , which is generally smaller than predicted. The derivative  $C_{n_\beta}$  decreases to a relatively low level at the higher angles of attack. Again, the power-on flight data are at a lower level of stability than the power-off flight data. Figures 15(b) and 16(b) show that  $C_{n_{\delta_r}}$  is lower than predicted. Figures 15(c) and 16(c) show  $C_{l_{\delta_a}}$  to be at the same level as or higher than predicted and  $C_{n_{\delta_a}}$  to be lower than predicted.

The trends of selected derivatives with Mach number are summarized in figure 17. Derivatives obtained from flight data in the angle of attack ranges from  $3.6^\circ$  to  $4.8^\circ$  and  $7^\circ$  to  $8.2^\circ$  are compared with interpolated power-off wind-tunnel predictions for  $4^\circ$  and  $7.5^\circ$ . At Mach numbers less than 1.35, power-off values of  $C_{l_\beta}$  were generally slightly smaller than predicted, whereas at Mach numbers greater than 1.35 the power-off values of  $C_{l_\beta}$  were slightly greater than predicted. Power-off values for  $C_{n_\beta}$  were greater than predictions for Mach numbers less than approximately 0.7 and equal to or less than predictions for higher Mach numbers. The power-on flight values for  $C_{l_\beta}$  and  $C_{n_\beta}$  were generally smaller than

the power-off flight values. The derivative  $C_{l_{\delta_a}}$  is usually slightly greater than predicted, with no apparent power effect. The derivative  $C_{n_{\delta_r}}$  is greater than predicted at Mach numbers less than approximately 1.3 but smaller than predicted at higher Mach numbers. Power had no apparent effect on  $C_{n_{\delta_r}}$ .

Discontinuities occurred in  $C_{n_\beta}$  with increasing Mach number near angles of attack of  $7.6^\circ$  and  $9.6^\circ$  (fig. 18). These nearly instantaneous changes in stability were correlated with step changes in pressure and visual observations of changes in flow patterns on the inboard side of the outboard vertical fins. These effects, which were not predicted, occurred as a function of Mach number and angle of attack.

Figure 19 is presented to give an indication of the spread of the data in an area of poor stability. The two flagged points are from maneuvers for which the match of the computed and measured time histories was poor. The resulting derivatives are not considered to be very reliable; however, it may not be possible to obtain better results because this area is traversed quickly and is difficult to analyze.

The reference 8 wind-tunnel predictions for a Mach number of 0.17 indicated that the gear-down values of  $C_{n_\beta}$  were unacceptably low. However, the gear-up predictions from reference 8 were also lower than the gear-up predictions from the subsonic (Mach 0.4) Cornell wind-tunnel tests. One gear-down maneuver was performed during the flare prior to landing and yielded the result presented in figure 20. Of primary importance is the high level of  $C_{n_\beta}$  that was obtained in flight with the gear down. However, a comparison of the flight gear-down data point with the flight gear-up data also shows that the effect of extending the gear on  $C_{n_\beta}$  appears to be approximately the same as the incremental effect predicted by the 0.17 Mach number wind-tunnel tests.

The side-force derivatives,  $C_{Y_\beta}$ ,  $C_{Y_{\delta_r}}$ , and  $C_{Y_{\delta_a}}$ , have not been discussed at length, because  $C_{Y_\beta}$  was always near predictions, and although  $C_{Y_{\delta_r}}$  and  $C_{Y_{\delta_a}}$  usually differed from the predictions, they rarely affect aircraft handling qualities.

## CONCLUSIONS

Estimates of the longitudinal and lateral-directional aerodynamic derivatives for the X-24B research aircraft were obtained from flight data by using a modified maximum likelihood estimation method. The flight derivatives were consistent and provided a good documentation of the aircraft's characteristics. The correlation between the flight and wind-tunnel data can be summarized as follows:

(1) The longitudinal static stability derivative,  $C_{m_\alpha}$ , was generally smaller than predicted. Some reductions due to power occurred, but the reductions were not consistent.

(2) The longitudinal control effectiveness derivative,  $C_{m_{\delta_e}}$ , was generally greater than predicted.

(3) The change in the coefficient of normal force due to angle of attack,  $C_{N_\alpha}$ , was smaller than the predictions based on untrimmed flight.

(4) At Mach numbers less than approximately 1.35, the power-off values for the lateral-directional static stability derivative,  $C_{l_\beta}$ , were generally slightly smaller than predicted. At higher Mach numbers, power-off values for  $C_{l_\beta}$  were generally slightly greater than predicted. The power-on flight values were smaller than the power-off values.

(5) At Mach numbers less than approximately 0.7, the power-off values for the lateral-directional static stability derivative,  $C_{n_\beta}$ , were higher than predicted. At higher Mach numbers, power-off values for  $C_{n_\beta}$  were smaller than predicted. Power-on flight values were smaller than the power-off values.

(6) The rudder control effectiveness derivative,  $C_{n_{\delta_r}}$ , was greater than predicted at Mach numbers below 1.3 and smaller than predicted at higher Mach numbers.

(7) The aileron control effectiveness derivative,  $C_{l_{\delta_a}}$ , was slightly greater than predicted.

(8) The yaw due to aileron derivative,  $C_{n_{\delta_a}}$ , was usually smaller than predicted.

*Dryden Flight Research Center  
National Aeronautics and Space Administration  
Edwards, California, 93523  
June 1, 1975*

## REFERENCES

1. Sim, Alex G.: Flight-Determined Stability and Control Characteristics of the M2-F3 Lifting Body Vehicle. NASA TN D-7511, 1973.
2. Sim, Alex G.: Results of a Feasibility Study Using the Newton-Raphson Digital Computer Program To Identify Lifting Body Derivatives From Flight Data. NASA TM X-56017, 1973.
3. Richardson, Norman R.; and Pearson, Albin O.: Wind-Tunnel Calibrations of a Combined Pitot-Static Tube, Vane-Type Flow-Direction Transmitter, and Stagnation-Temperature Element at Mach Numbers From 0.60 to 2.87. NASA TN D-122, 1959.
4. Maine, Richard E.; and Iliff, Kenneth W.: A FORTRAN Program for Determining Aircraft Stability and Control Derivatives From Flight Data. NASA TN D-7831, 1975.
5. Iliff, Kenneth W.; and Taylor, Lawrence W., Jr.: Determination of Stability Derivatives From Flight Data Using a Newton-Raphson Minimization Technique. NASA TN D-6579, 1972.
6. Jenke, Leroy M.: Wind Tunnel Tests of an FDL-8X Double-Delta Spacecraft Model at Mach Numbers From 1.5 to 8.0. AEDC-TR-71-218, Arnold Eng. Dev. Center, Oct. 1971.
7. Lindsay, E. Earl: Aerodynamic Characteristics of the AFFDL X-24B Configuration at Mach Numbers From 1.5 to 5.0—Final Report, Feb. 14–19, 1977. AD-922716L ARO-VKF-TR-74-58, Air Force Flight Dynamics Lab., Sept. 1974. (Reference corrected from initial publication.)
8. Norris, Richard B.; Sotomayer, William A.; and Fehl, John E.: Parametric Study of an 8% Scale Model of the X-24B in the Landing Configuration. AFFDL-TM-73-21-FXS, Air Force Flight Dynamics Lab., Apr. 1973.

Table 1. Physical characteristics of X-24B research aircraft.

Body -												
Reference planform area, m <sup>2</sup> (ft <sup>2</sup> )	.	.	.	.	.	.	.	.	.	.	.	30.704 (330.50)
Reference longitudinal length, m (ft)	.	.	.	.	.	.	.	.	.	.	.	11.43 (37.50)
Reference span, m (ft)	.	.	.	.	.	.	.	.	.	.	.	5.791 (19.00)
Leading edge sweep, deg	.	.	.	.	.	.	.	.	.	.	.	78
Outboard vertical fins, each -												
Area, m <sup>2</sup> (ft <sup>2</sup> )	.	.	.	.	.	.	.	.	.	.	.	2.406 (25.90)
Root chord, m (ft)	.	.	.	.	.	.	.	.	.	.	.	2.578 (8.46)
Tip chord, m (ft)	.	.	.	.	.	.	.	.	.	.	.	1.054 (3.46)
Span, m (ft)	.	.	.	.	.	.	.	.	.	.	.	1.273 (4.18)
Leading edge sweep, deg	.	.	.	.	.	.	.	.	.	.	.	55
Center fin -												
Area, m <sup>2</sup> (ft <sup>2</sup> )	.	.	.	.	.	.	.	.	.	.	.	1.366 (14.70)
Root chord, m (ft)	.	.	.	.	.	.	.	.	.	.	.	1.877 (6.16)
Tip chord, m (ft)	.	.	.	.	.	.	.	.	.	.	.	0.965 (3.17)
Span, m (ft)	.	.	.	.	.	.	.	.	.	.	.	0.985 (3.23)
Leading edge sweep, deg	.	.	.	.	.	.	.	.	.	.	.	55
Strake -												
Area, m <sup>2</sup> (ft <sup>2</sup> )	.	.	.	.	.	.	.	.	.	.	.	2.897 (31.18)
Chord, m (ft)	.	.	.	.	.	.	.	.	.	.	.	2.860 (9.38)
Span, m (ft)	.	.	.	.	.	.	.	.	.	.	.	1.267 (4.16)
Leading edge sweep, deg	.	.	.	.	.	.	.	.	.	.	.	72
Ailerons, each -												
Area, m <sup>2</sup> (ft <sup>2</sup> )	.	.	.	.	.	.	.	.	.	.	.	1.369 (14.74)
Chord, m (ft)	.	.	.	.	.	.	.	.	.	.	.	1.212 (3.98)
Span, m (ft)	.	.	.	.	.	.	.	.	.	.	.	1.267 (4.16)
Bias deflection, deg	.	.	.	.	.	.	.	.	.	.	.	3 to 11
Deflection from bias position, deg	.	.	.	.	.	.	.	.	.	.	.	±5
Upper flaps, each -												
Area, m <sup>2</sup> (ft <sup>2</sup> )	.	.	.	.	.	.	.	.	.	.	.	1.005 (10.82)
Chord, m (ft)	.	.	.	.	.	.	.	.	.	.	.	0.866 (2.84)
Span, m (ft)	.	.	.	.	.	.	.	.	.	.	.	1.161 (3.81)
Deflection, deg	.	.	.	.	.	.	.	.	.	.	.	0 to -60
Lower flaps, each -												
Area, m <sup>2</sup> (ft <sup>2</sup> )	.	.	.	.	.	.	.	.	.	.	.	1.300 (13.99)
Chord, m (ft)	.	.	.	.	.	.	.	.	.	.	.	1.140 (3.74)
Span, m (ft)	.	.	.	.	.	.	.	.	.	.	.	1.140 (3.74)
Deflection, deg	.	.	.	.	.	.	.	.	.	.	.	0 to 40

Table 1. Concluded.

Upper rudders, each -														
Area m <sup>2</sup> (ft <sup>2</sup> )	.	.	.	.	.	.	.	.	.	.	.	.	.	0.464 (4.99)
Chord, m (ft)	.	.	.	.	.	.	.	.	.	.	.	.	.	0.752 (2.47)
Span, m (ft)	.	.	.	.	.	.	.	.	.	.	.	.	.	0.615 (2.02)
Bias deflection, deg	.	.	.	.	.	.	.	.	.	.	.	.	.	±10
Deflection from bias position, deg	.	.	.	.	.	.	.	.	.	.	.	.	.	±15
Lower rudders, each -														
Area, m <sup>2</sup> (ft <sup>2</sup> )	.	.	.	.	.	.	.	.	.	.	.	.	.	0.620 (6.67)
Chord, m (ft)	.	.	.	.	.	.	.	.	.	.	.	.	.	0.752 (2.47)
Span, m (ft)	.	.	.	.	.	.	.	.	.	.	.	.	.	0.823 (2.70)
Bias deflection, deg	.	.	.	.	.	.	.	.	.	.	.	.	.	±10

Table 2. Typical variation of moments of inertia and center of gravity with gross weight.

Gross weight, kg (lb)	$I_X$ , kg-m <sup>2</sup> (slug-ft <sup>2</sup> )	$I_Y$ , kg-m <sup>2</sup> (slug-ft <sup>2</sup> )	$I_Z$ , kg-m <sup>2</sup> (slug-ft <sup>2</sup> )	$I_{XZ}$ , kg-m <sup>2</sup> (slug-ft <sup>2</sup> )	Center of gravity, per $\bar{c}$
6,260 (13,800)	4,352 (3,210)	33,720 (24,870)	34,670 (25,570)	1,120 (829)	0.6616
5,810 (12,800)	4,181 (3,084)	33,480 (24,690)	34,380 (25,360)	1,060 (785)	0.6600
5,350 (11,800)	4,051 (2,988)	33,330 (24,580)	34,150 (25,190)	1,030 (760)	0.6577
4,850 (10,700)	3,921 (2,892)	33,180 (24,470)	33,900 (25,000)	982 (724)	0.6536
4,350 (9,600)	3,747 (2,764)	32,810 (24,200)	33,450 (24,670)	944 (696)	0.6510
3,860 (8,500)	3,592 (2,650)	32,150 (23,710)	32,700 (24,120)	841 (620)	0.6421



E-26620

Figure 1. X-24B research aircraft in flight.



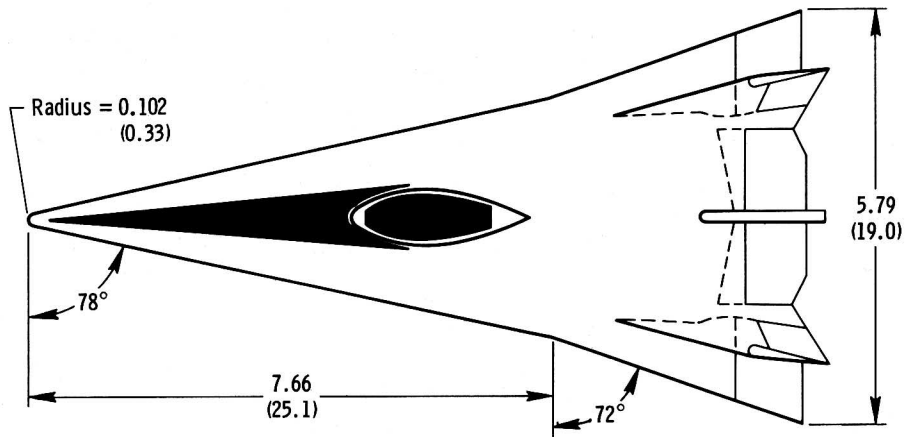
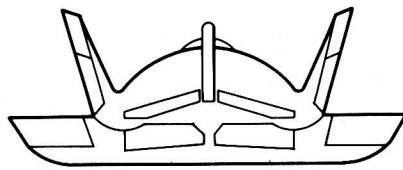
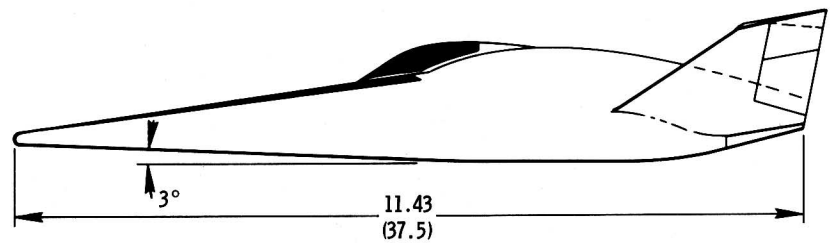


Figure 2. X-24B research aircraft dimensions (in meters (feet)).

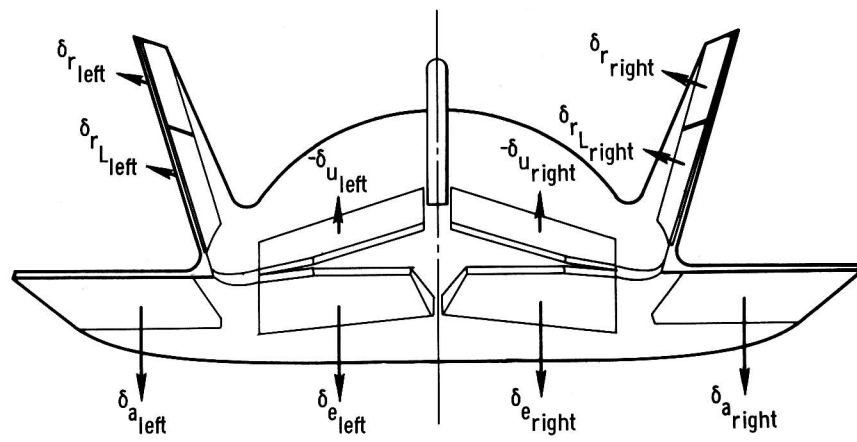
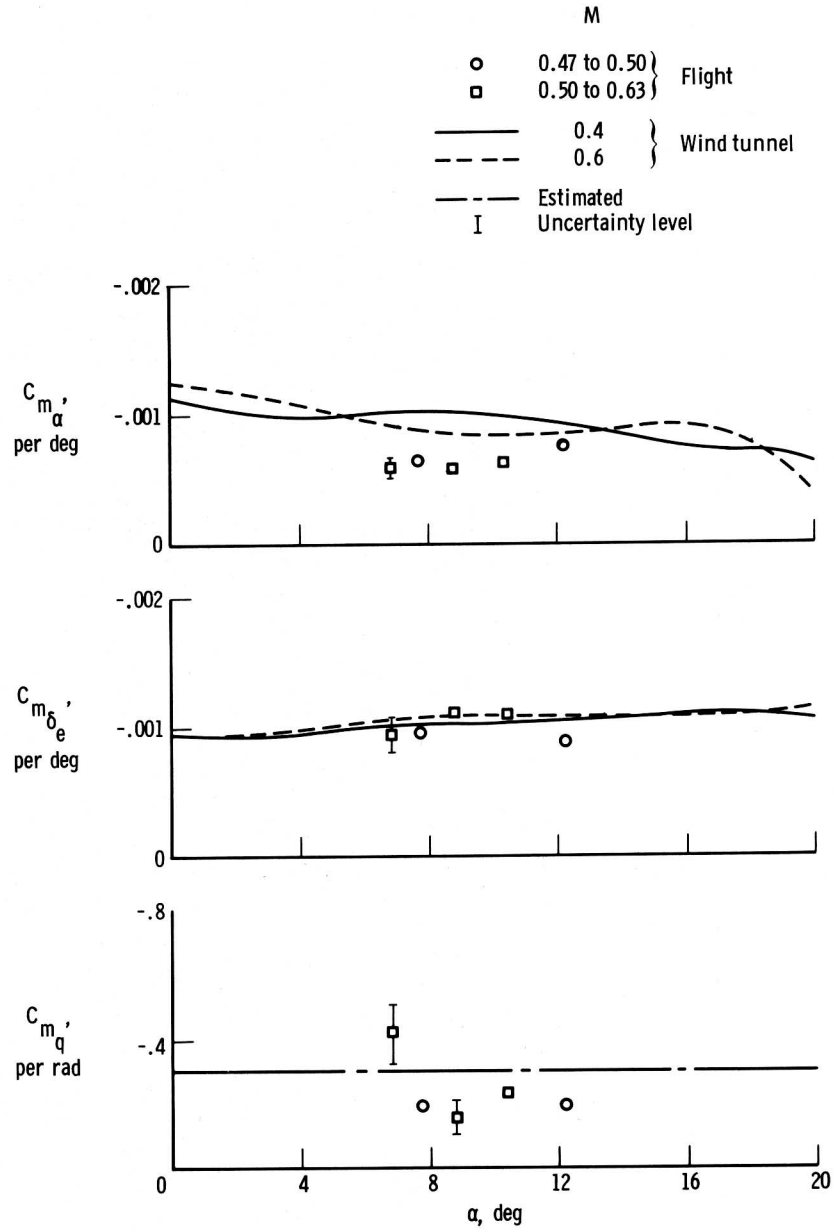
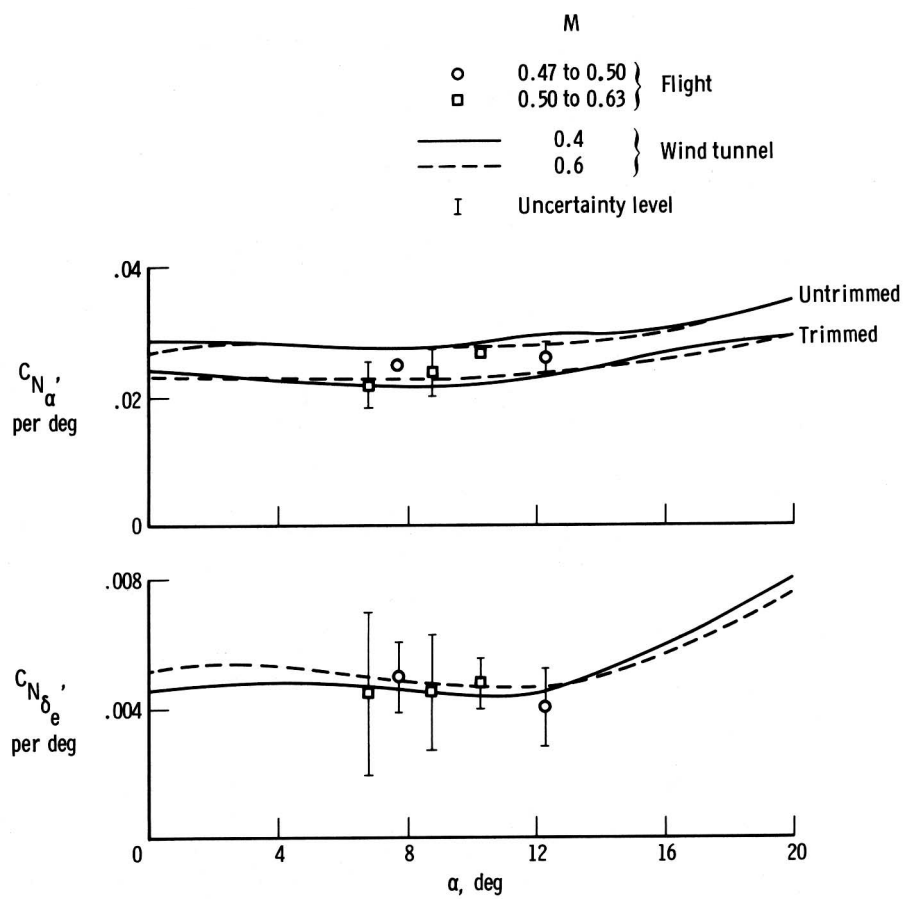


Figure 3. Control surface location and sign convention.



(a)  $C_{m_\alpha}$ ,  $C_{m_{\delta_e}}$ ,  $C_{m_q}$ .

Figure 4. Comparison of longitudinal derivatives obtained from flight data with wind-tunnel results.  $M = 0.47$  to  $0.63$ ; subsonic configuration; center of gravity =  $0.66\bar{c}$ .



(b)  $C_{N_\alpha}$ ,  $C_{N_{\delta_e}}$

Figure 4. Concluded.

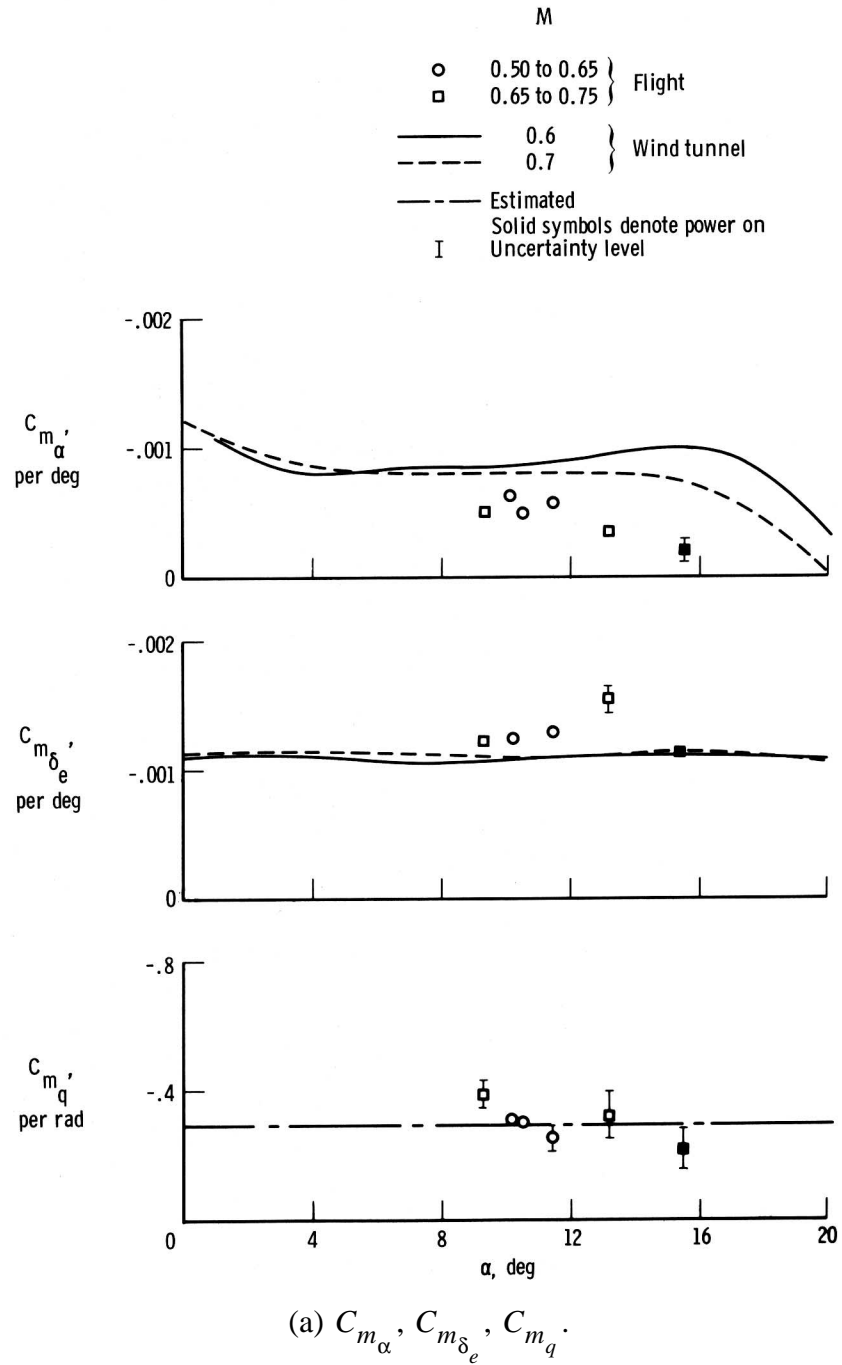
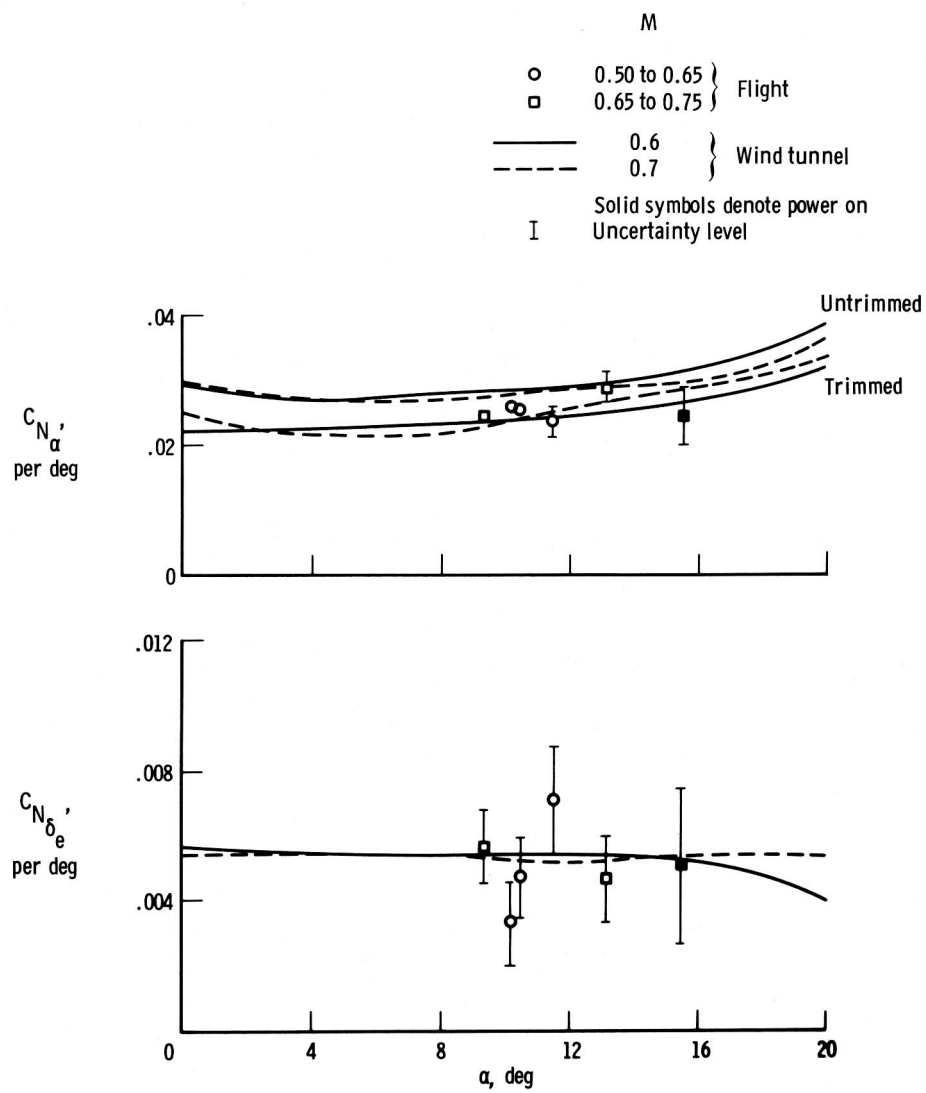


Figure 5. Comparison of longitudinal derivatives obtained from flight data with wind-tunnel results.  $M = 0.50$  to  $0.75$ ; transonic configuration; center of gravity =  $0.66\bar{c}$ .



(b)  $C_{N_\alpha}$ ,  $C_{N_{\delta_e}}$ .

Figure 5. Concluded.

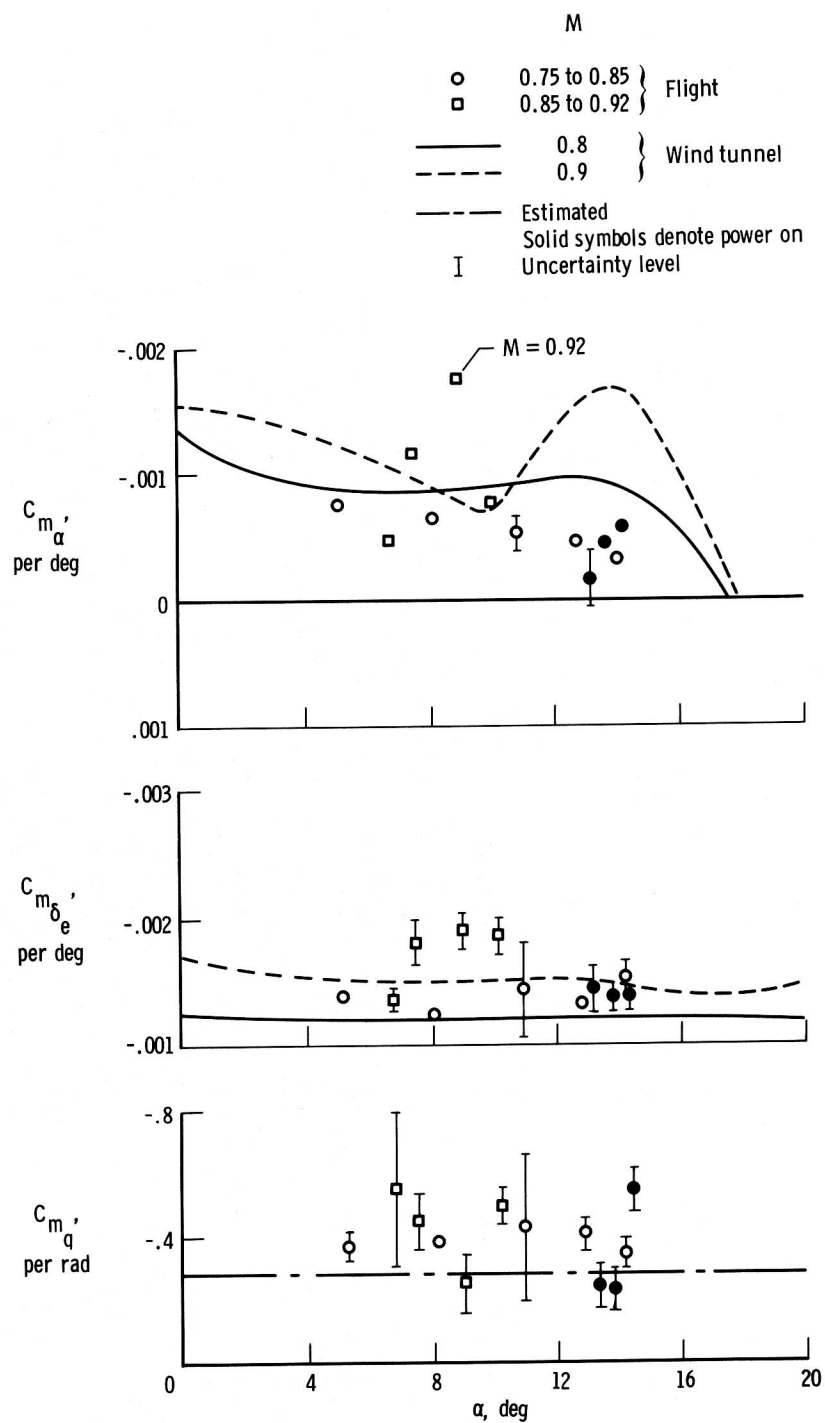
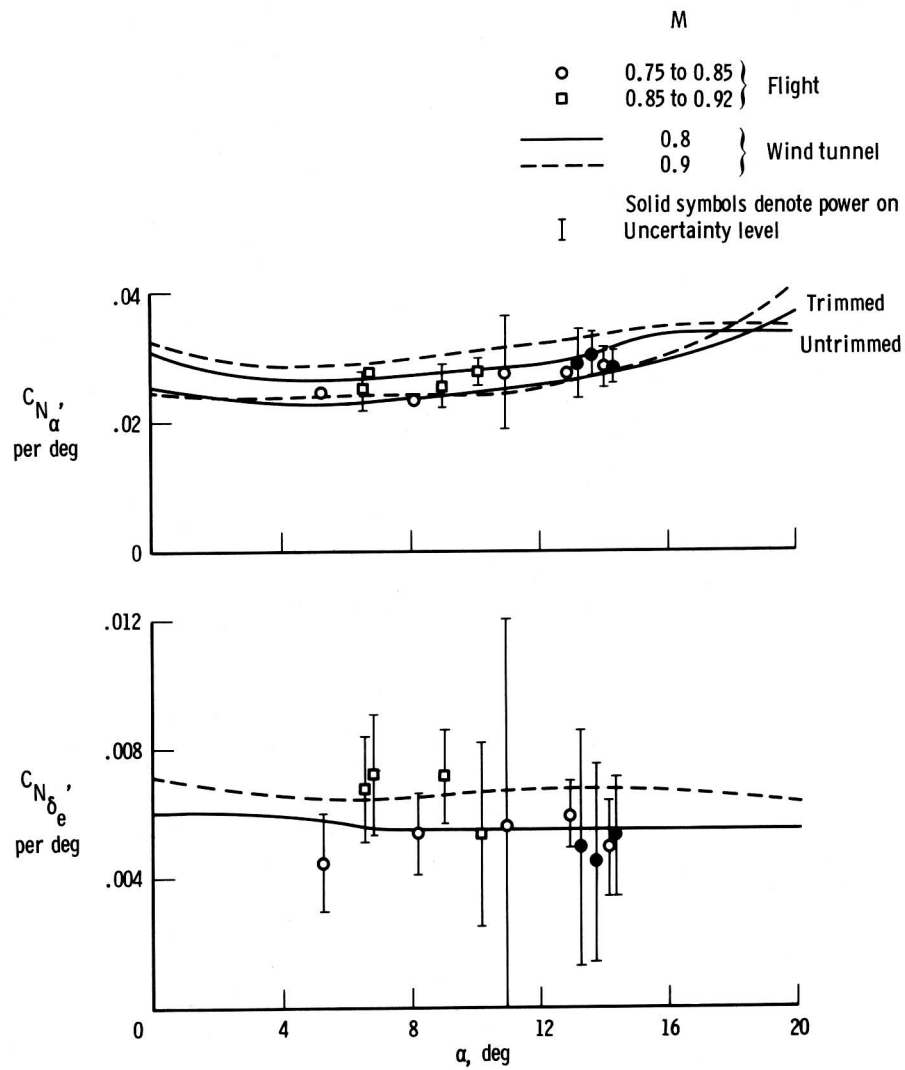


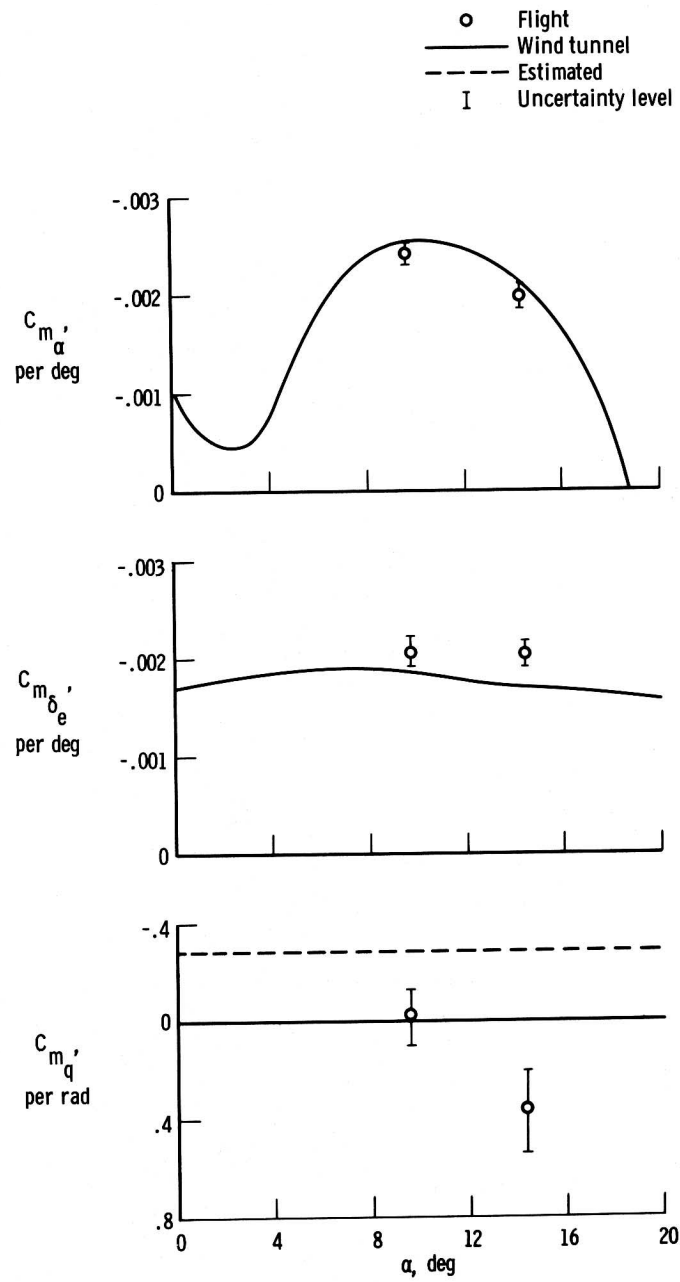
Figure 6. Comparison of longitudinal derivatives obtained from flight data with wind-tunnel results.  $M = 0.75$  to  $0.92$ ; transonic configuration; center of gravity =  $0.66\bar{c}$ .



(b)  $C_{N_{\alpha}}, C_{N_{\delta_e}}$

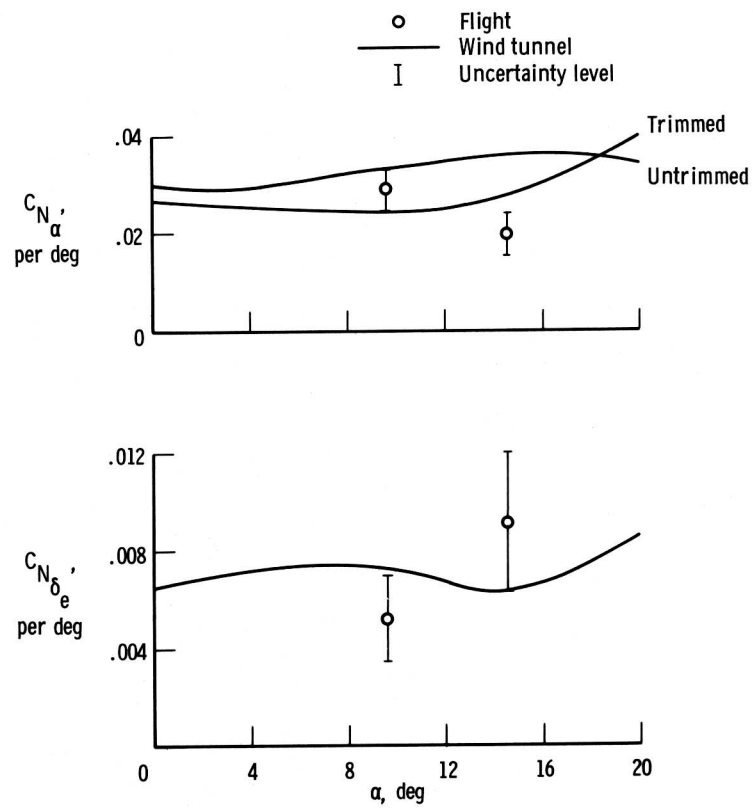
Figure 6. Concluded.





(a)  $C_{m_\alpha}$ ,  $C_{m_{\delta_e}}$ ,  $C_{m_q}$ .

Figure 7. Comparison of longitudinal derivatives obtained from flight data with wind-tunnel results.  $M = 0.95$ ; transonic configuration; center of gravity =  $0.66\bar{c}$ .



(b)  $C_{N_{\alpha}}$ ,  $C_{N_{\delta_e}}$ .

Figure 7. Concluded.

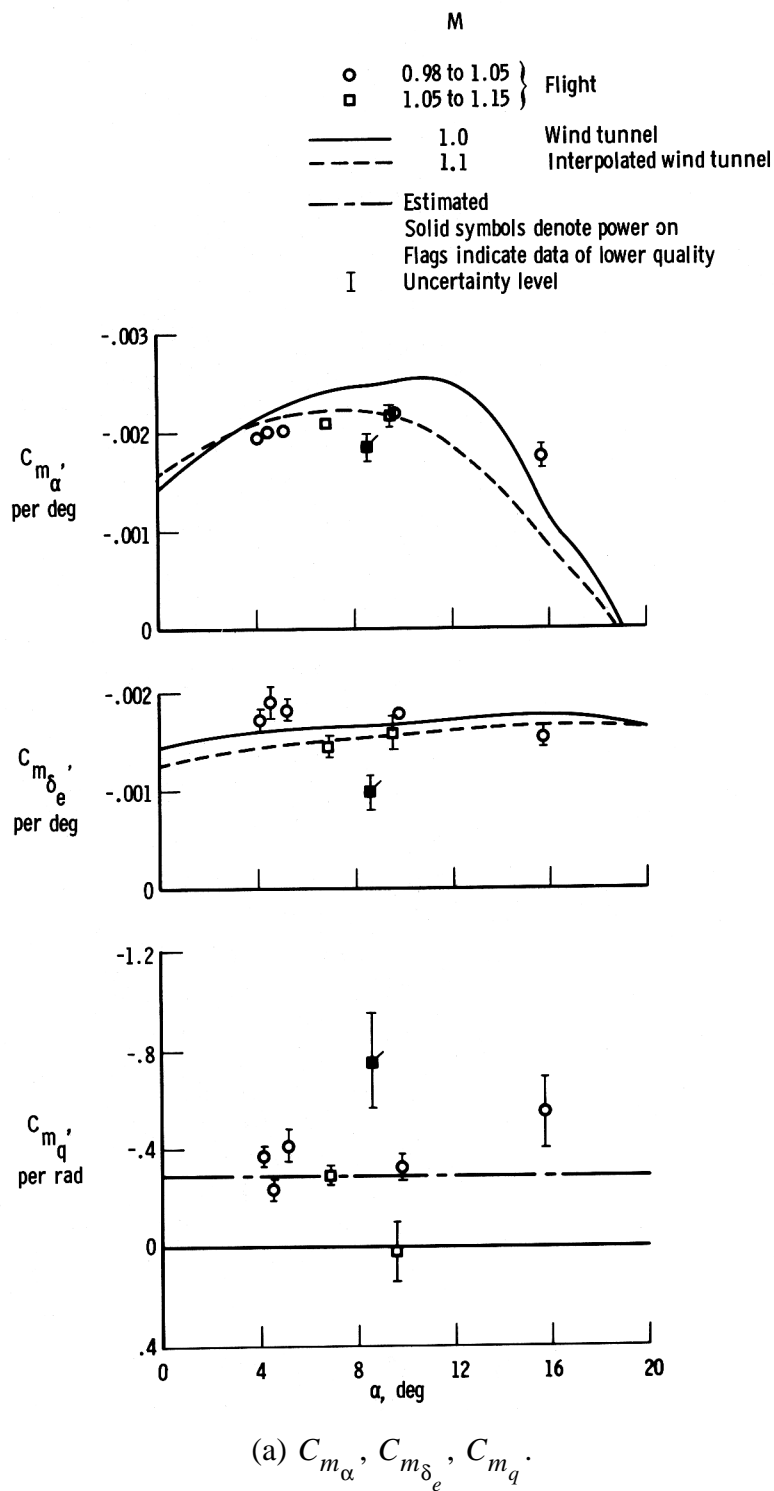
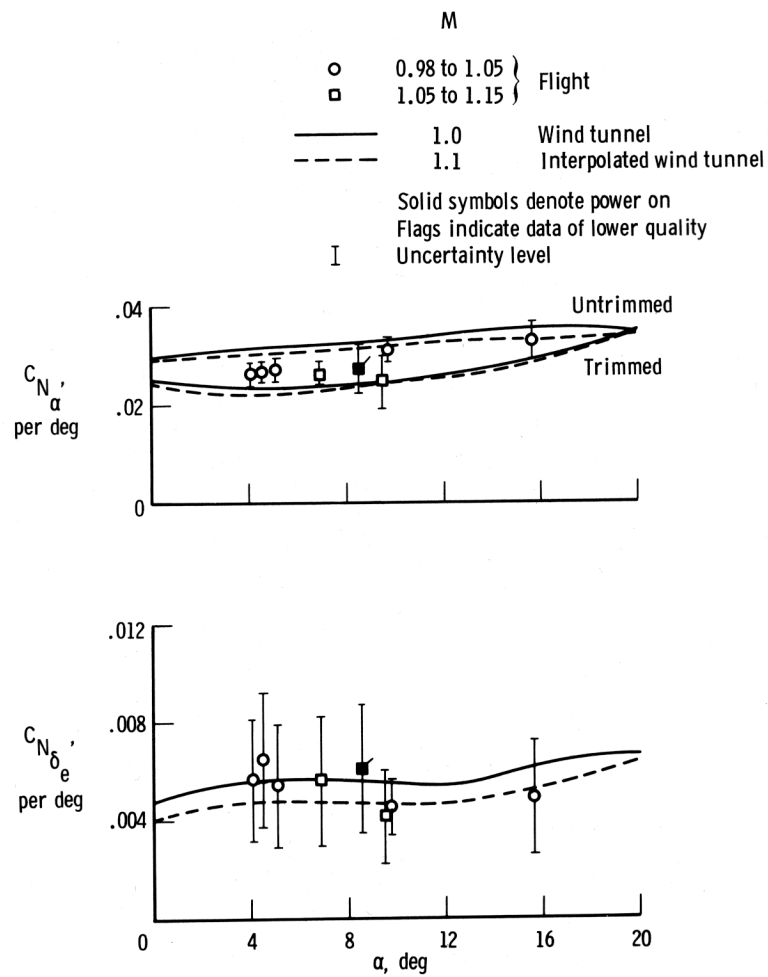


Figure 8. Comparison of longitudinal derivatives obtained from flight data with wind-tunnel results.  $M = 0.98$  to  $1.15$ ; transonic configuration; center of gravity  $= 0.66\bar{c}$ .



(b)  $C_{N_\alpha}$ ,  $C_{N_{\delta_e}}$

Figure 8. Concluded.

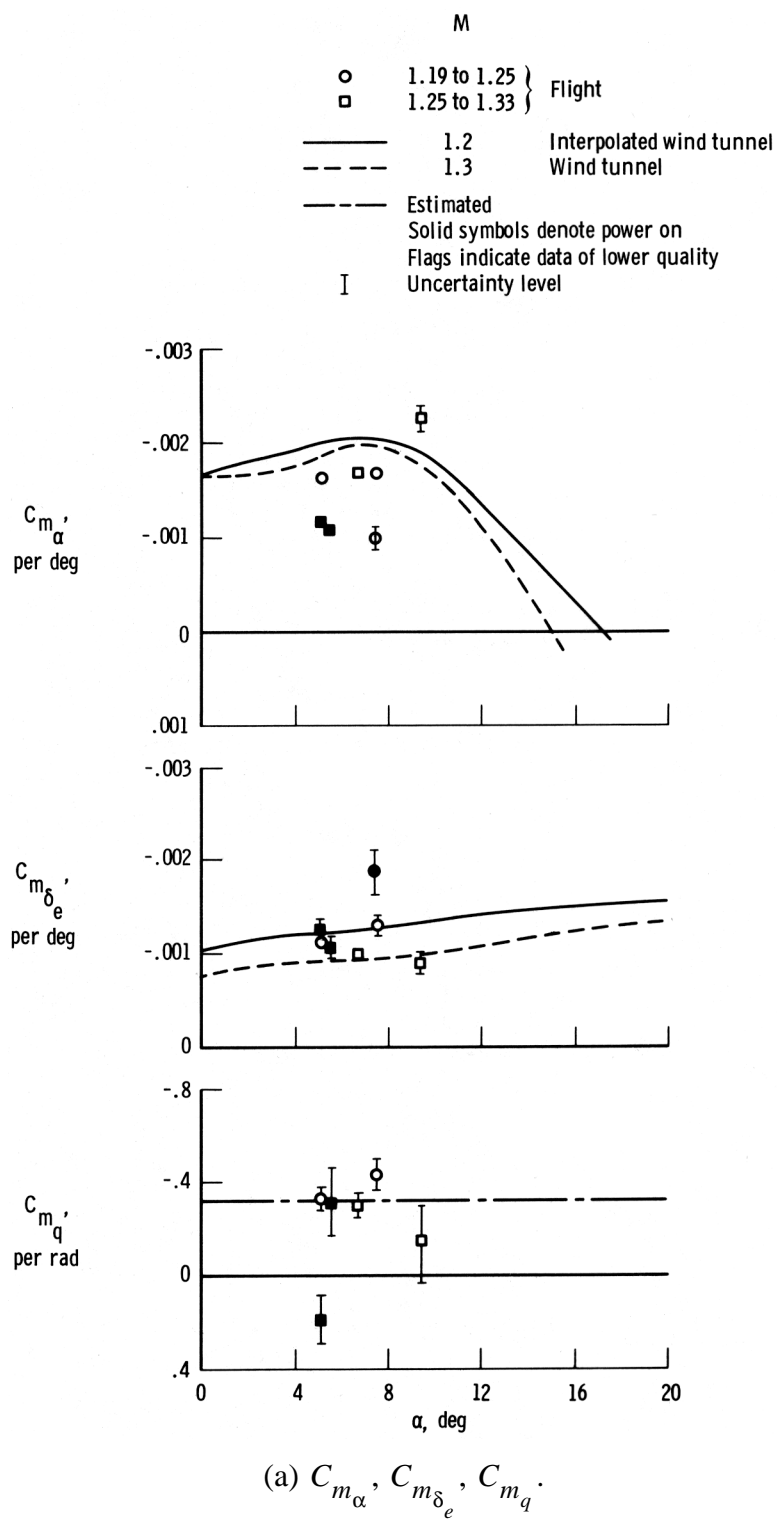
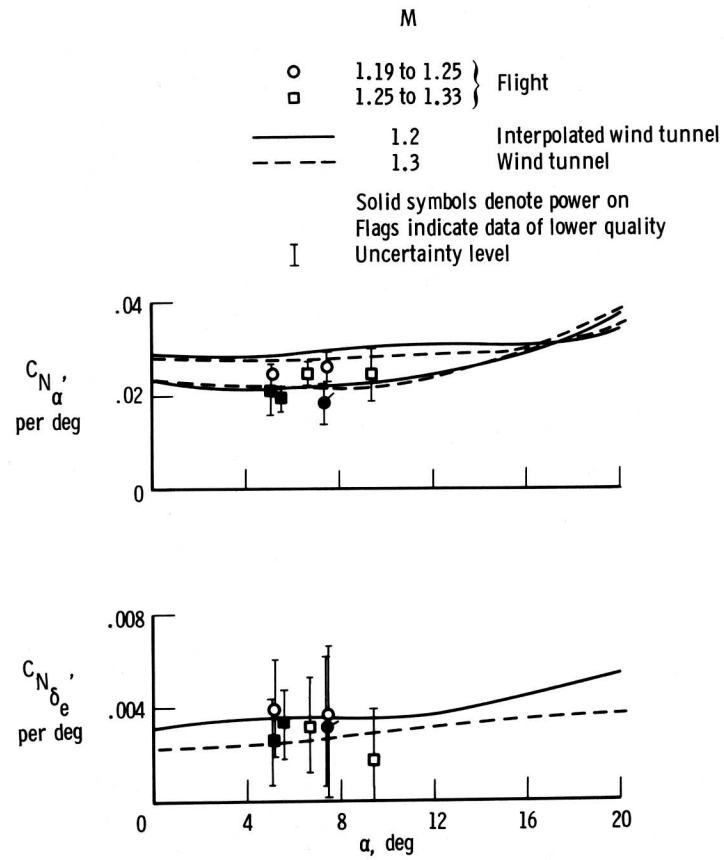
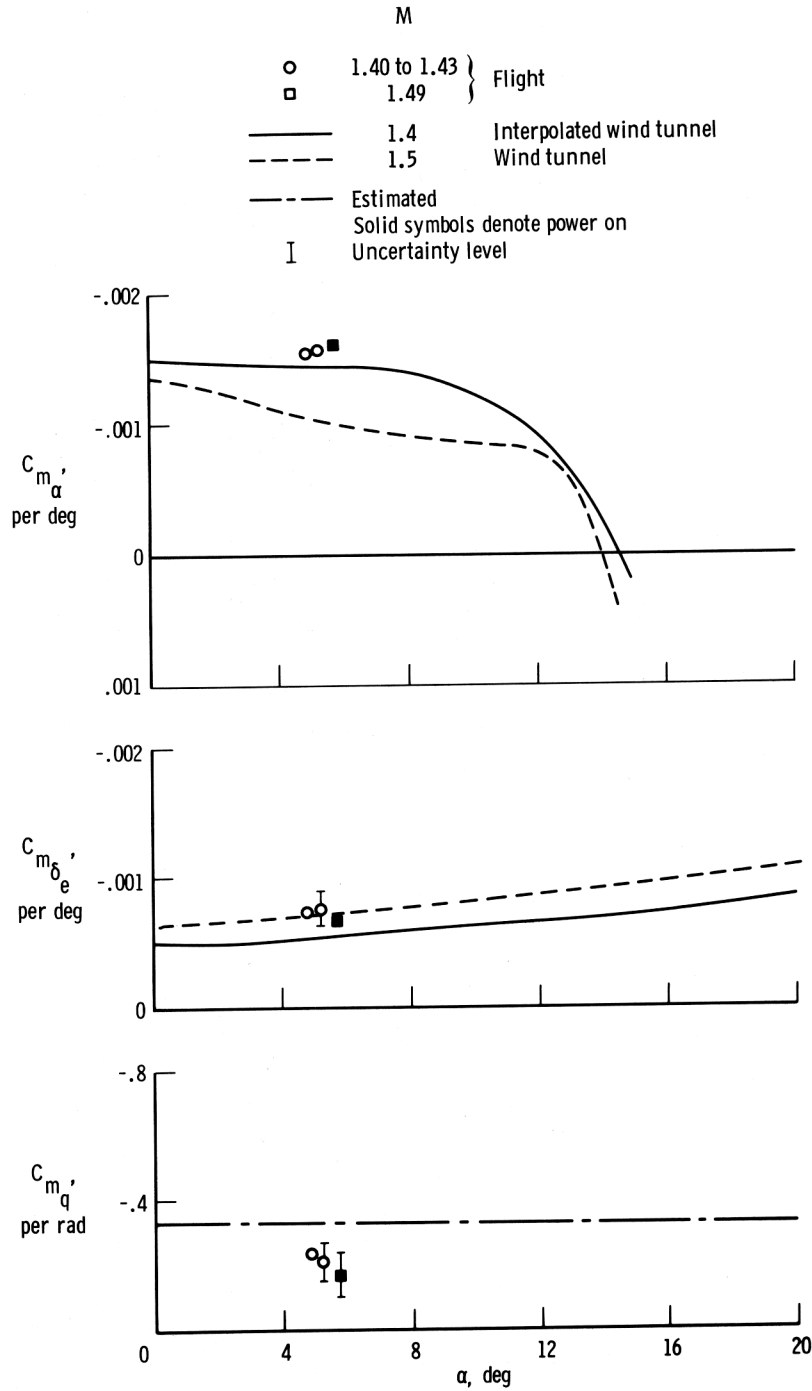


Figure 9. Comparison of longitudinal derivatives obtained from flight data with wind-tunnel results.  $M = 1.19$  to  $1.33$ ; transonic configuration; center of gravity =  $0.66\bar{c}$ .



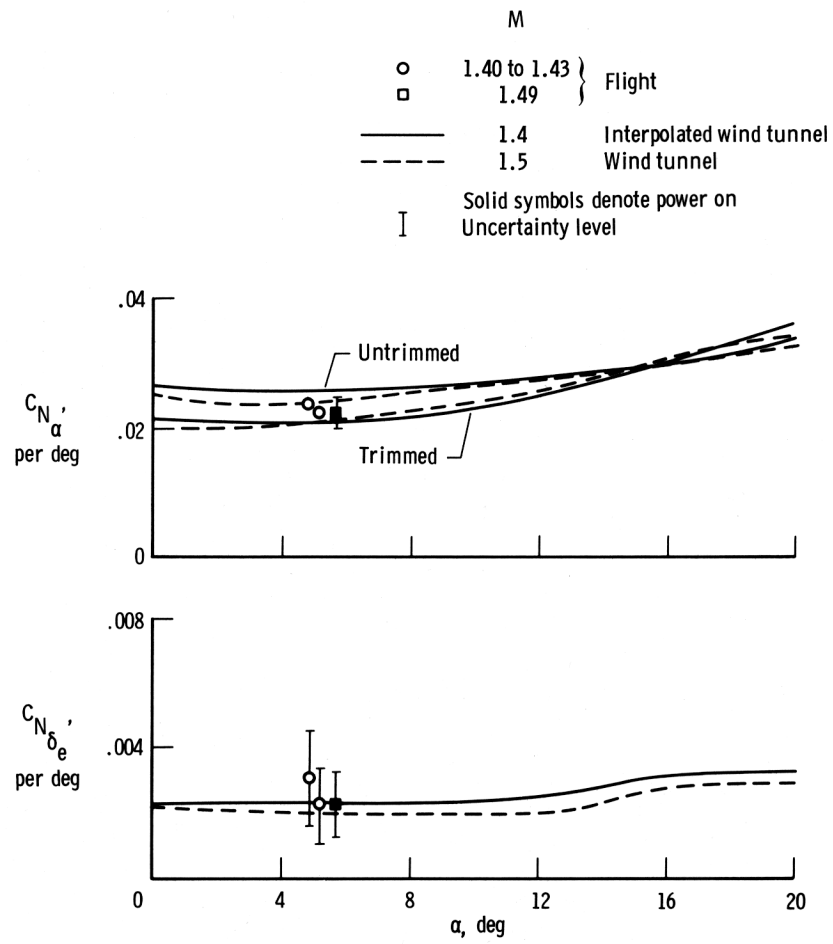
(b)  $C_{N_\alpha}$ ,  $C_{N_{\delta_e}}$

Figure 9. Concluded.



(a)  $C_{m_\alpha}$ ,  $C_{m_{\delta_e}}$ ,  $C_{m_q}$ .

Figure 10. Comparison of longitudinal derivatives obtained from flight data with wind-tunnel results.  $M = 1.40$  to  $1.49$ ; transonic configuration; center of gravity =  $0.66\bar{c}$ .



(b)  $C_{N_\alpha}$ ,  $C_{N_{\delta_e}}$

Figure 10. Concluded.



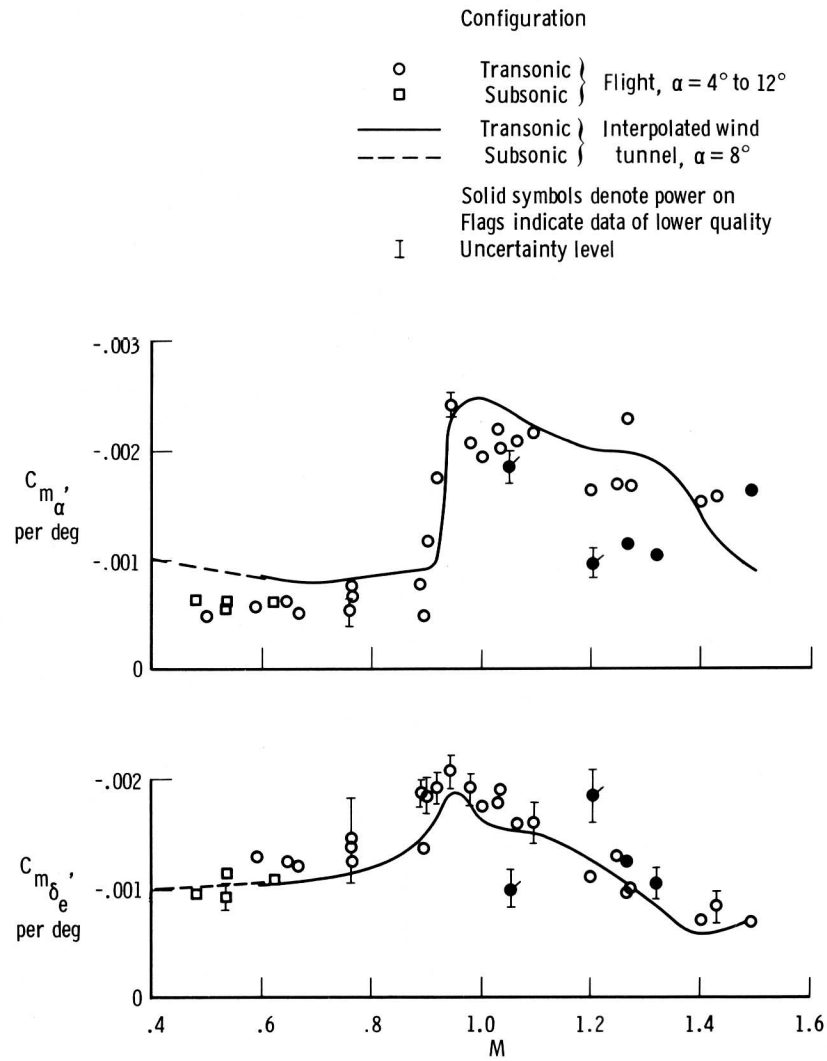
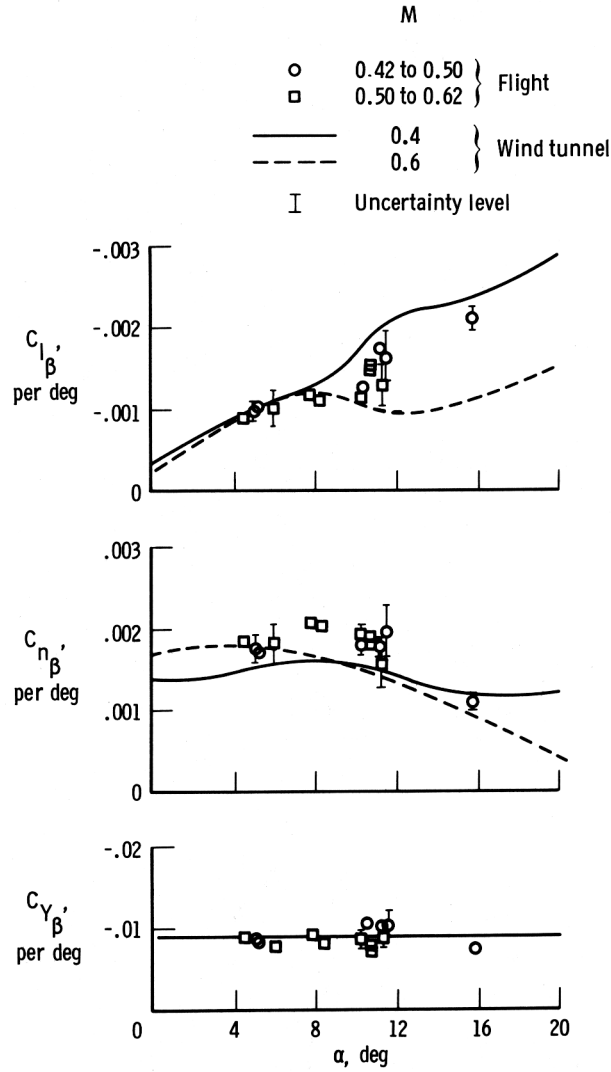
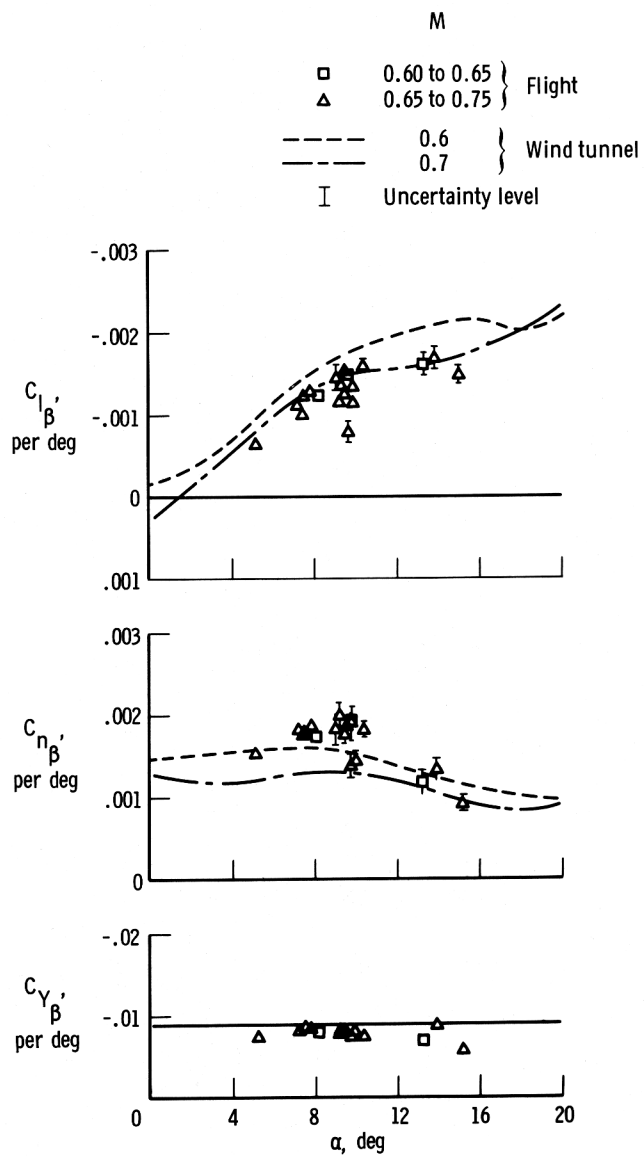


Figure 11. Comparison of longitudinal derivatives obtained from flight data with wind-tunnel results.  $\alpha = 4^\circ$  to  $12^\circ$ ; center of gravity =  $0.66\bar{c}$ .



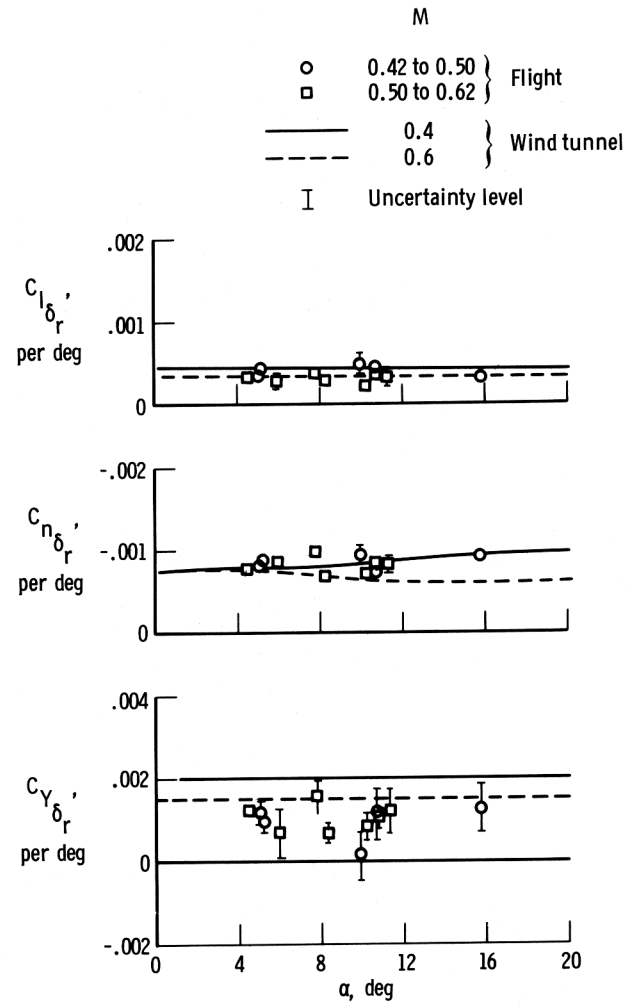
(a)  $C_{l_\beta}$ ,  $C_{n_\beta}$ ,  $C_{Y_\beta}$  for subsonic configuration.

Figure 12. Comparison of lateral-directional derivatives obtained from flight data with wind-tunnel results.  $M = 0.42$  to  $0.75$ ; center of gravity =  $0.65\bar{c}$ .



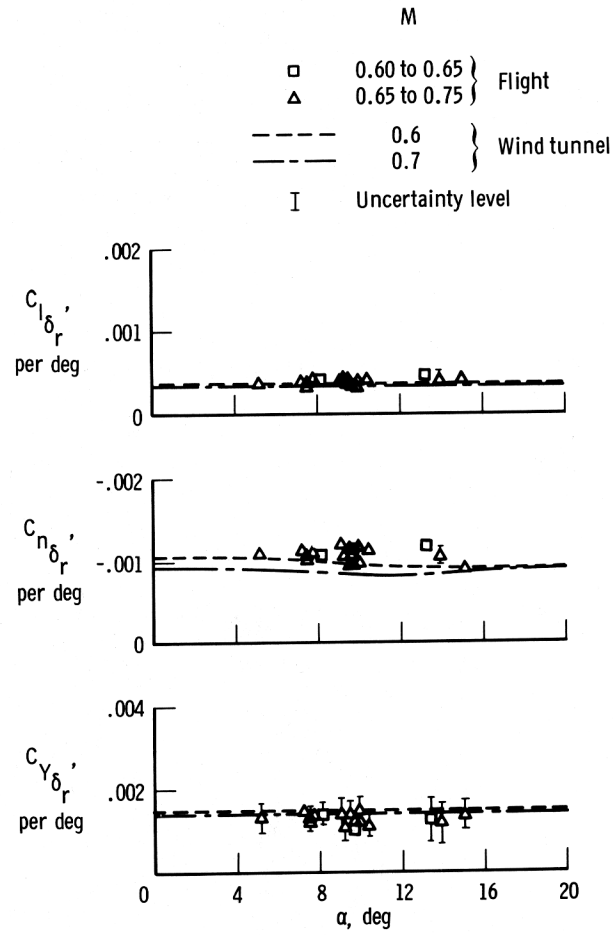
(b)  $C_{l_\beta}$ ,  $C_{n_\beta}$ ,  $C_{Y_\beta}$  for transonic configuration.

Figure 12. Continued.



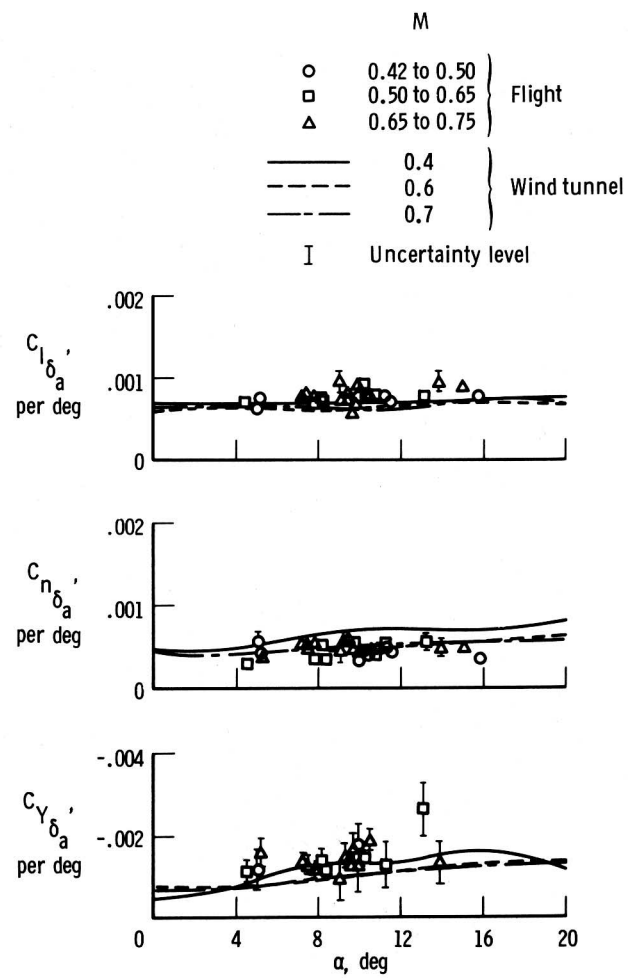
(c)  $C_{l_{\delta_r}}$ ,  $C_{n_{\delta_r}}$ ,  $C_{Y_{\delta_r}}$  for subsonic configuration.

Figure 12. Continued.



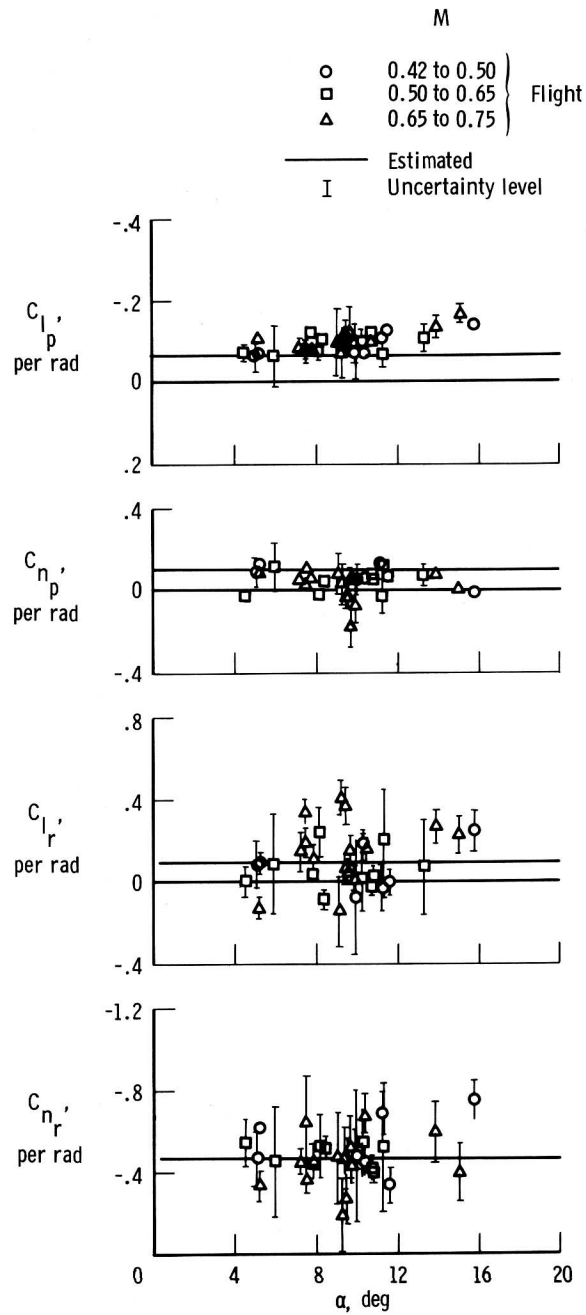
(d)  $C_{l_{\delta_r}}$ ,  $C_{n_{\delta_r}}$ ,  $C_{Y_{\delta_r}}$  for transonic configuration.

Figure 12. Continued.



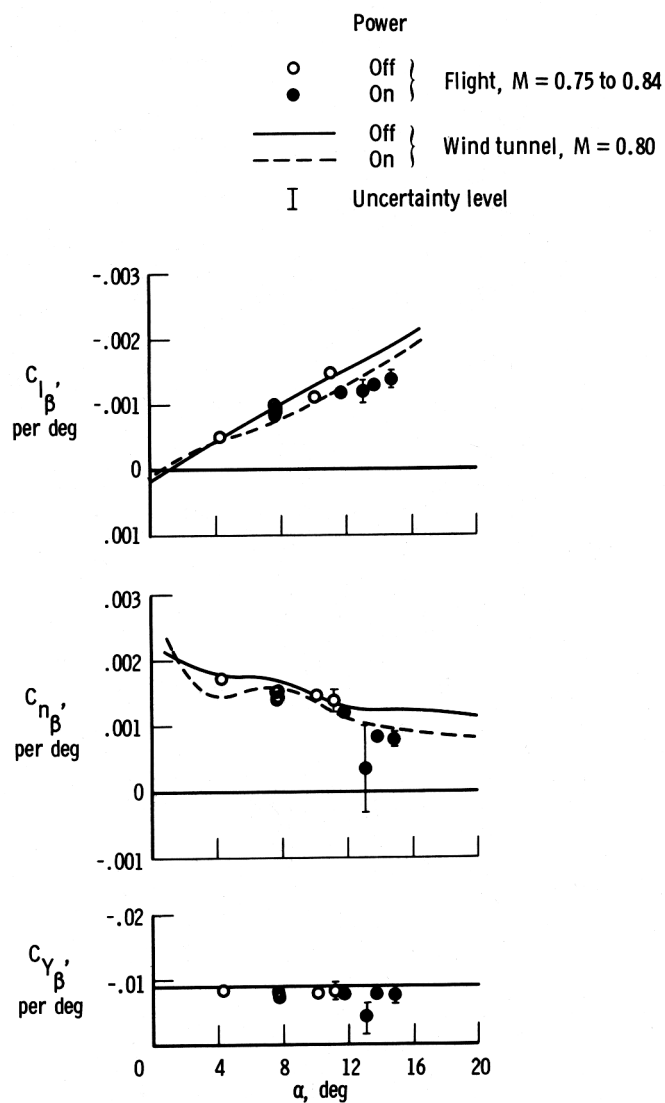
(e)  $C_{l_{\delta_a}}$ ,  $C_{n_{\delta_a}}$ ,  $C_{Y_{\delta_a}}$  for subsonic and transonic configurations.

Figure 12. Continued.



(f)  $C_{l_p}$ ,  $C_{n_p}$ ,  $C_{l_r}$ ,  $C_{n_r}$  for subsonic and transonic configurations.

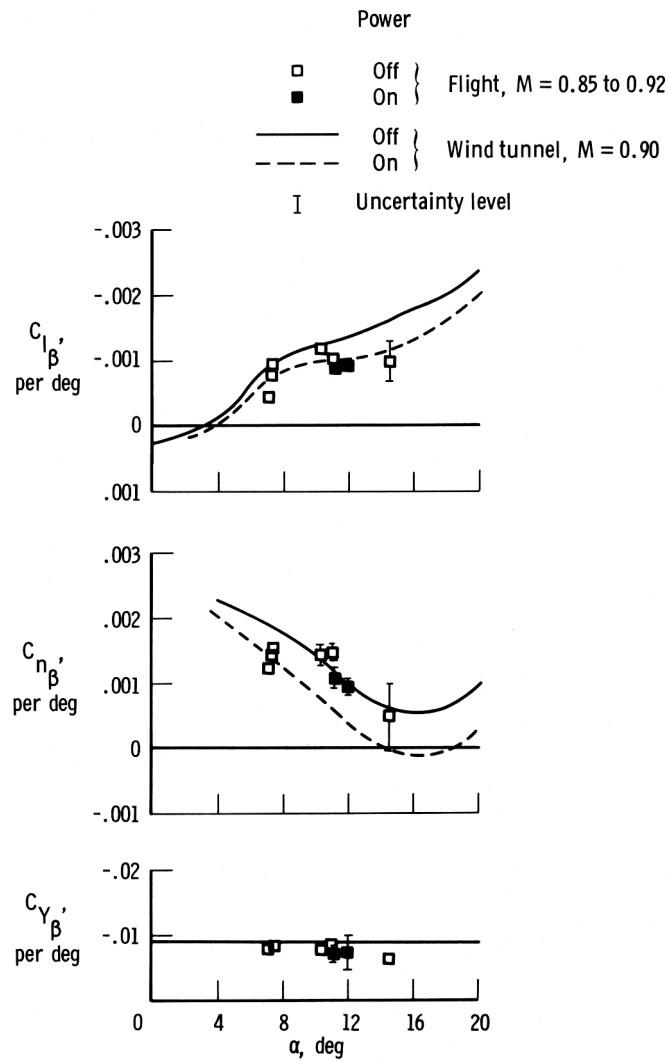
Figure 12. Concluded.



(a)  $C_{l_\beta}$ ,  $C_{n_\beta}$ ,  $C_{Y_\beta}$ .

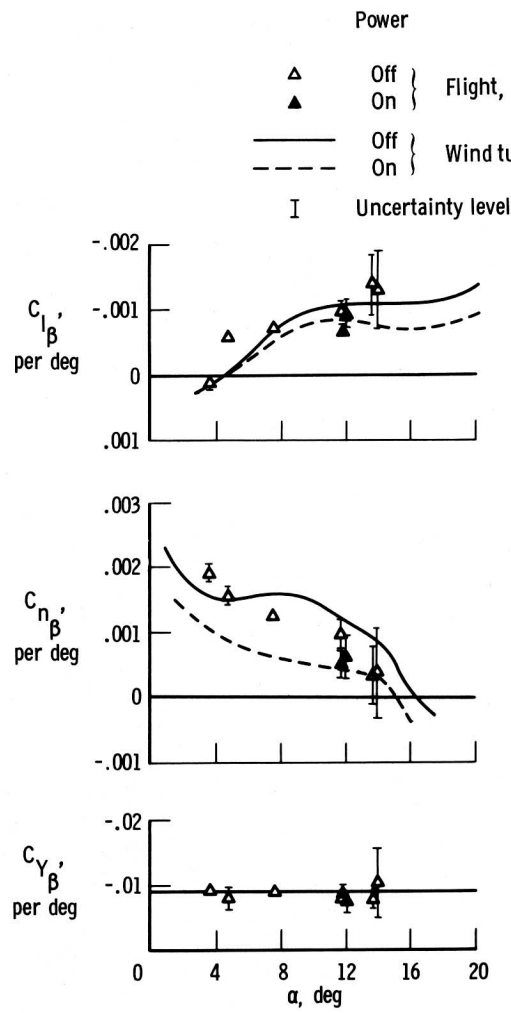
Figure 13. Comparison of lateral-directional derivatives obtained from flight data with wind-tunnel results.  $M = 0.75$  to  $0.98$ ; transonic configuration; center of gravity =  $0.65 \bar{c}$ .





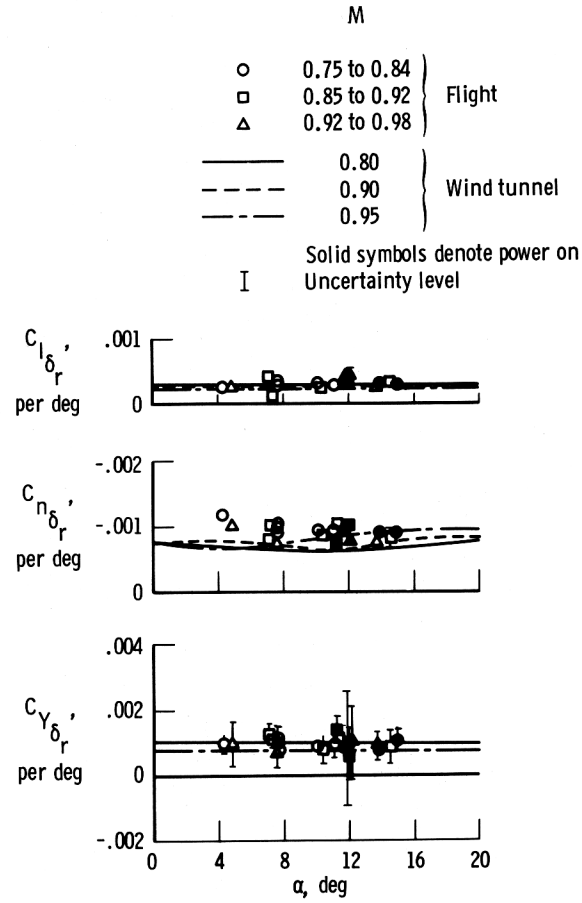
(a) Continued.

Figure 13. Continued.



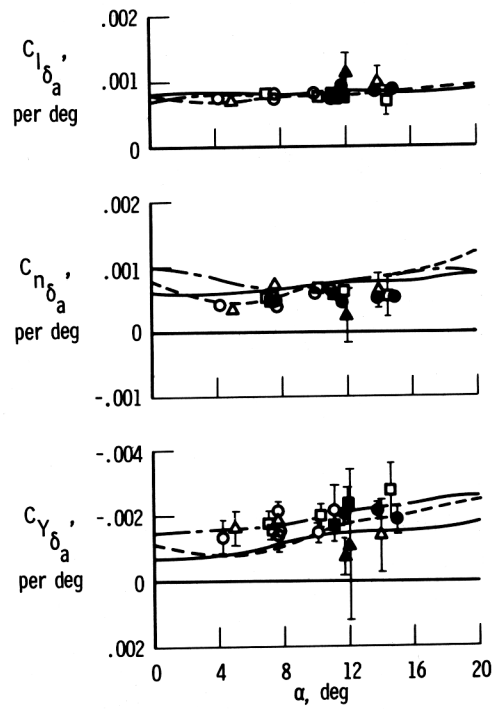
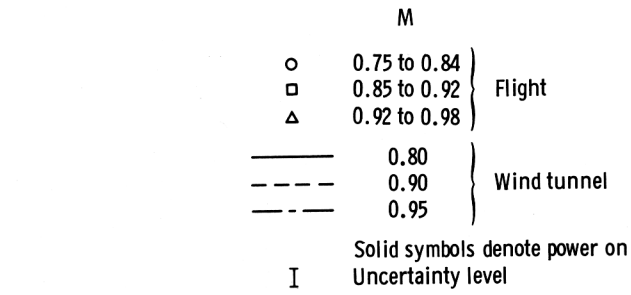
(a) Concluded.

Figure 13. Continued.



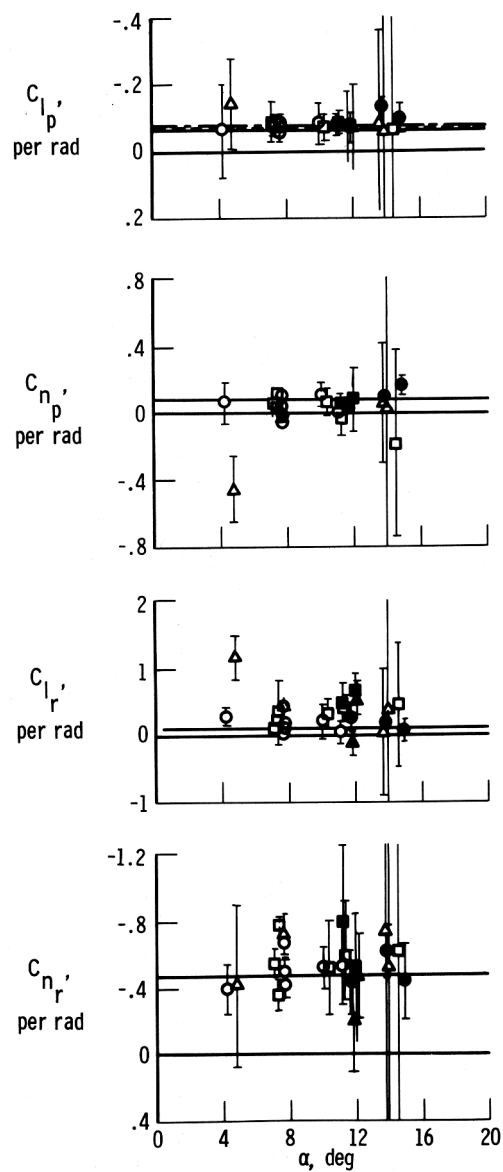
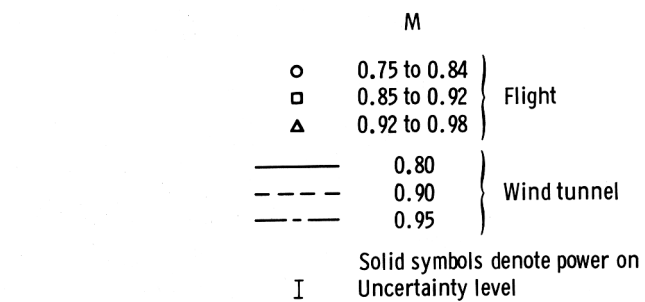
(b)  $C_{l_{\delta_r}}$ ,  $C_{n_{\delta_r}}$ ,  $C_{Y_{\delta_r}}$ .

Figure 13. Continued.



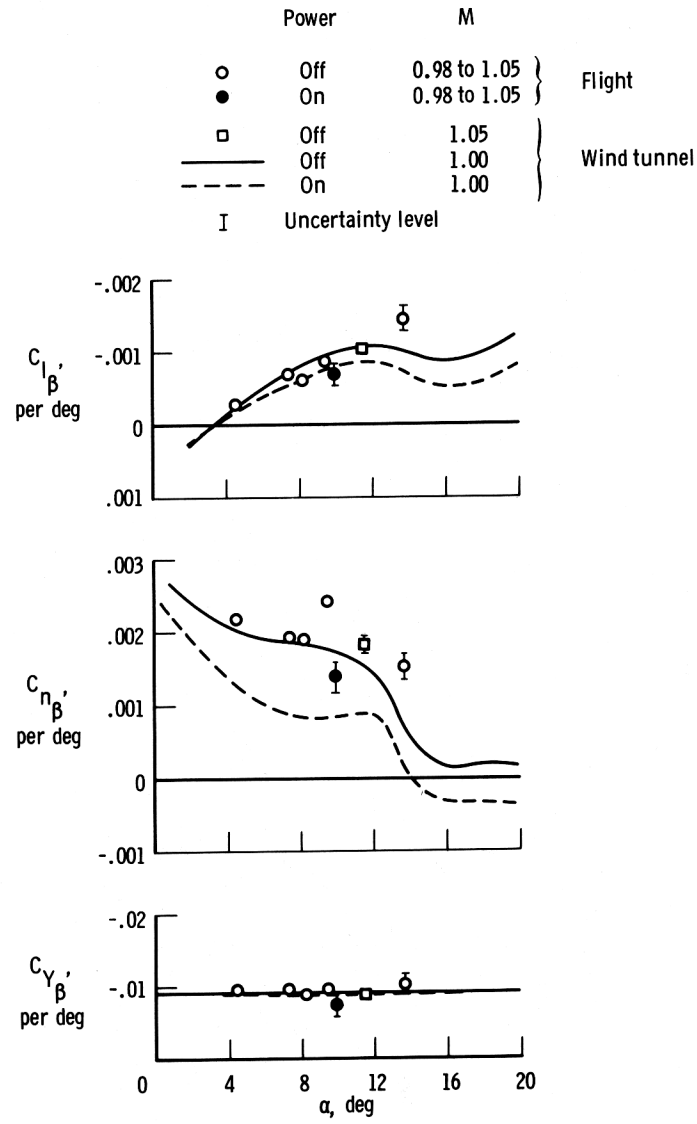
(c)  $C_{l_{\delta_a}}, C_{n_{\delta_a}}, C_{Y_{\delta_a}}$ .

Figure 13. Continued.



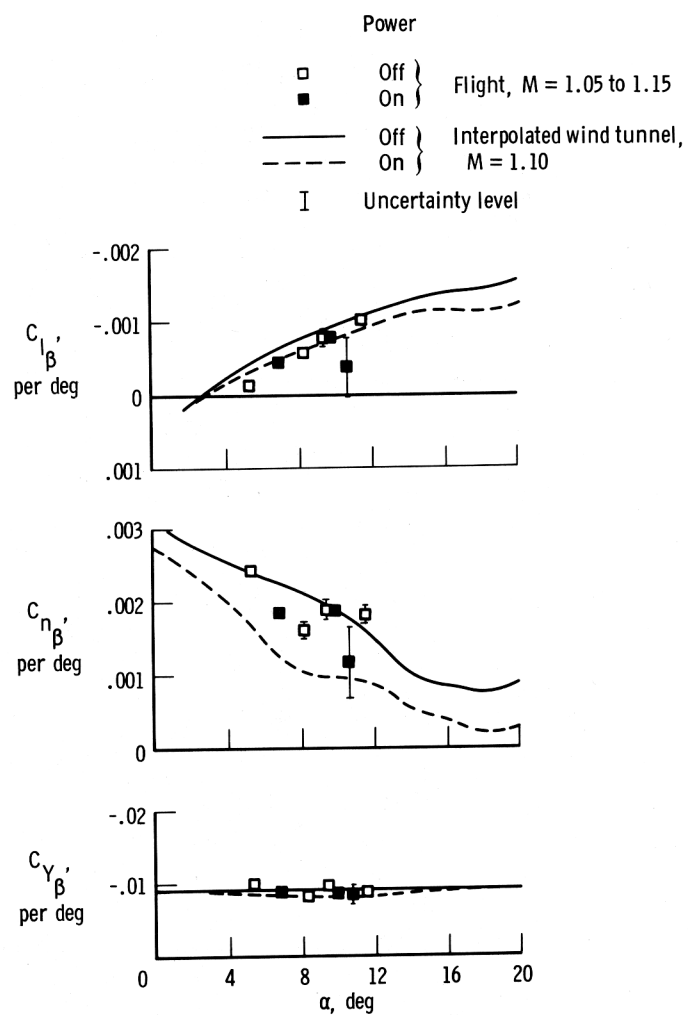
(d)  $C_{l_p}$ ,  $C_{n_p}$ ,  $C_{l_r}$ ,  $C_{n_r}$ .

Figure 13. Concluded.



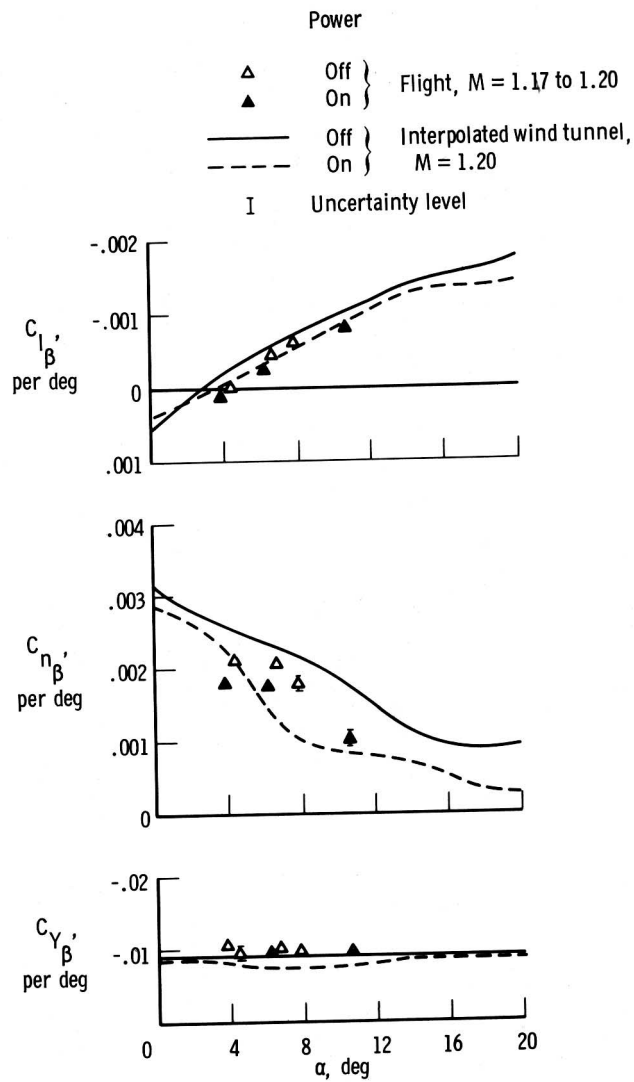
(a)  $C_{l_\beta}$ ,  $C_{n_\beta}$ ,  $C_{Y_\beta}$ .

Figure 14. Comparison of lateral-directional derivatives obtained from flight data with wind-tunnel results.  $M = 0.98$  to  $1.20$ ; transonic configuration; center of gravity =  $0.65 \bar{c}$ .



(a) Continued.

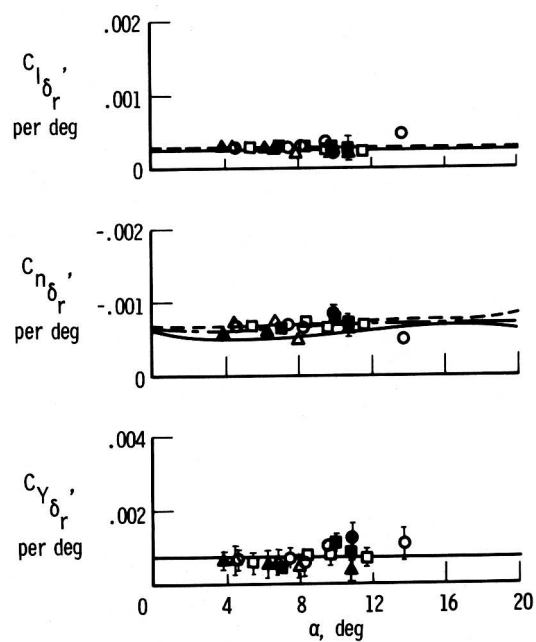
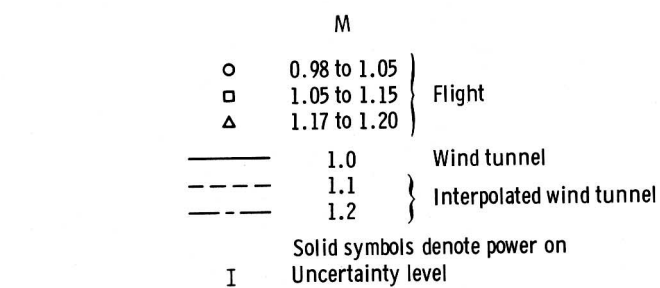
Figure 14. Continued.



(a) Concluded.

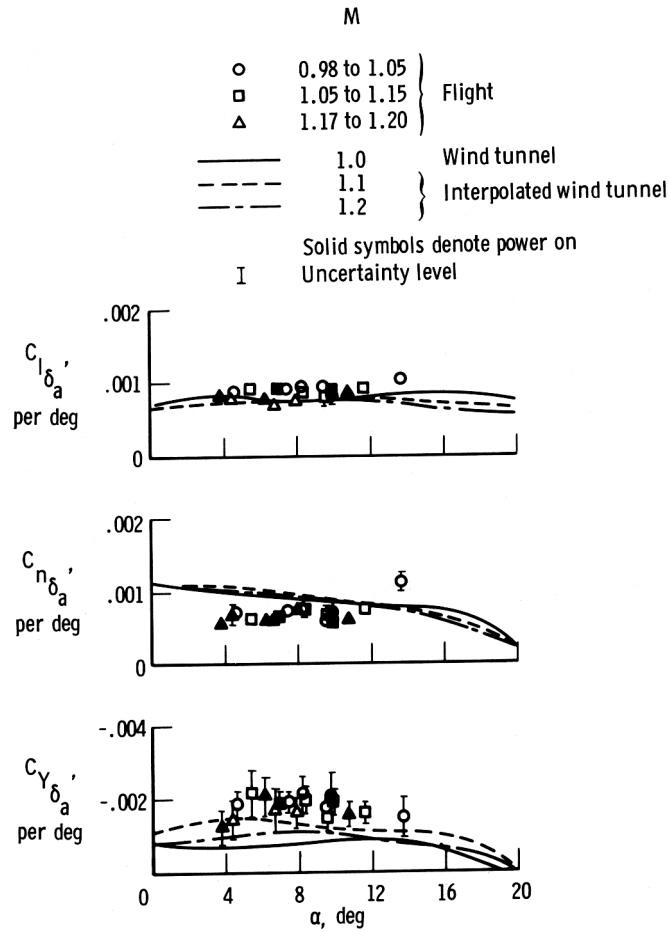
Figure 14. Continued.





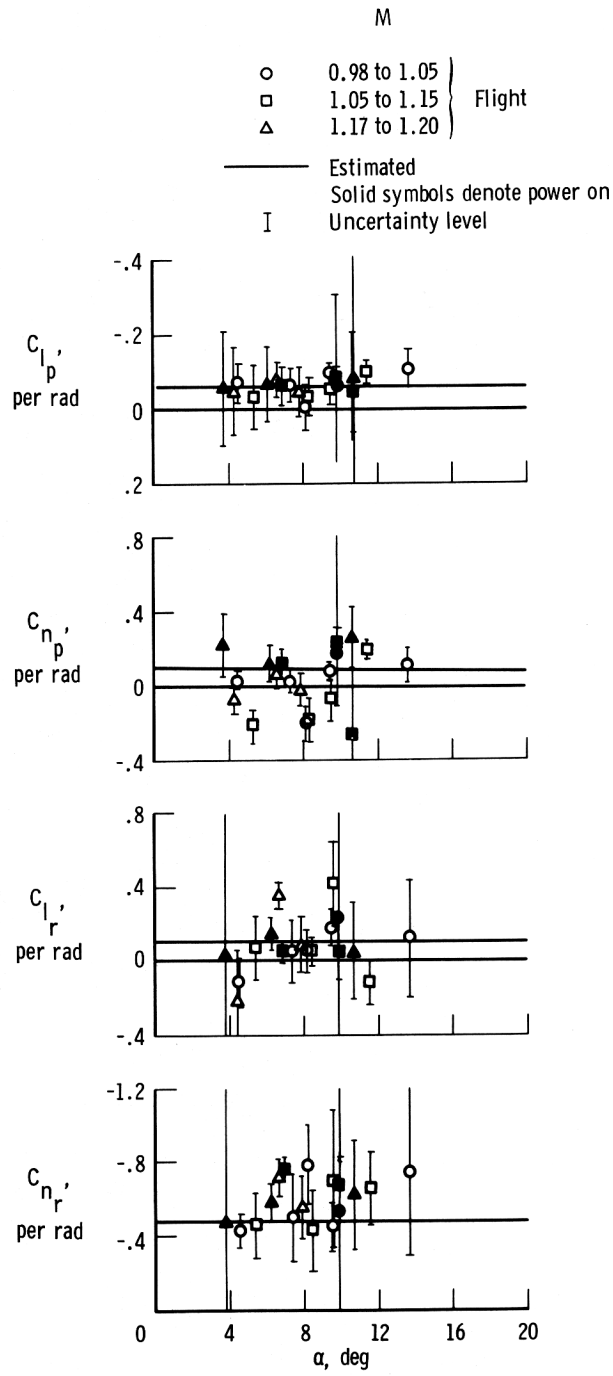
(b)  $C_{l_{\delta_r}}, C_{n_{\delta_r}}, C_{Y_{\delta_r}}$ .

Figure 14. Continued.



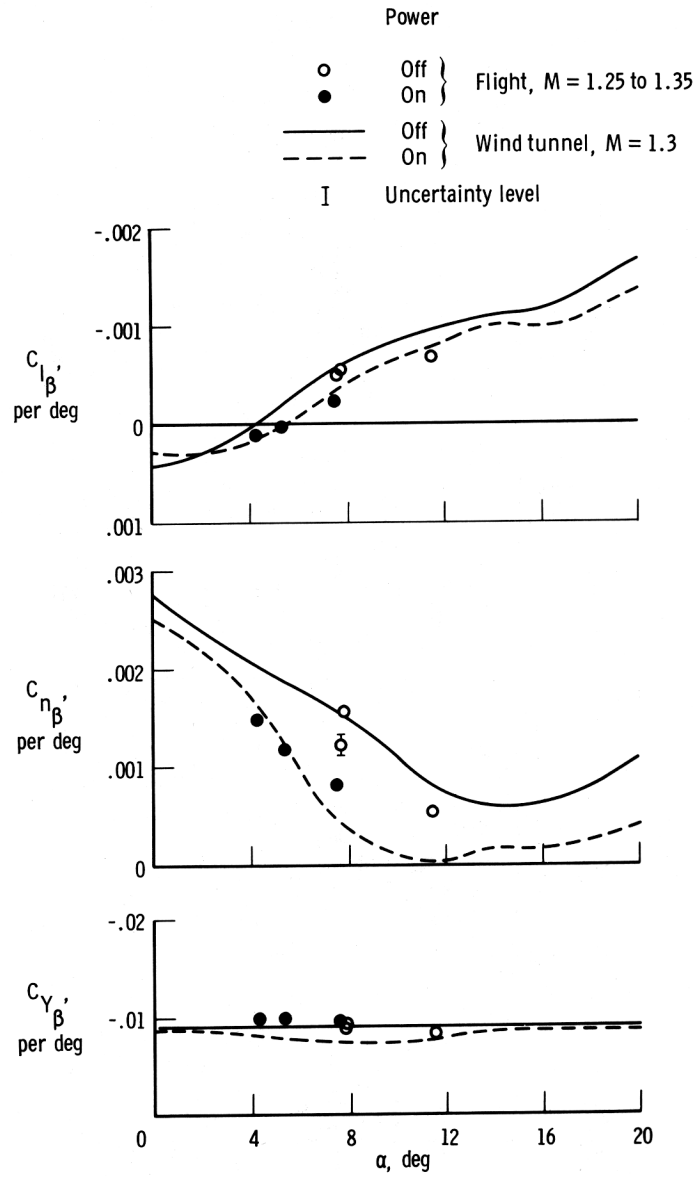
(c)  $C_{l_{\delta_a}}$ ,  $C_{n_{\delta_a}}$ ,  $C_{Y_{\delta_a}}$ .

Figure 14. Continued.



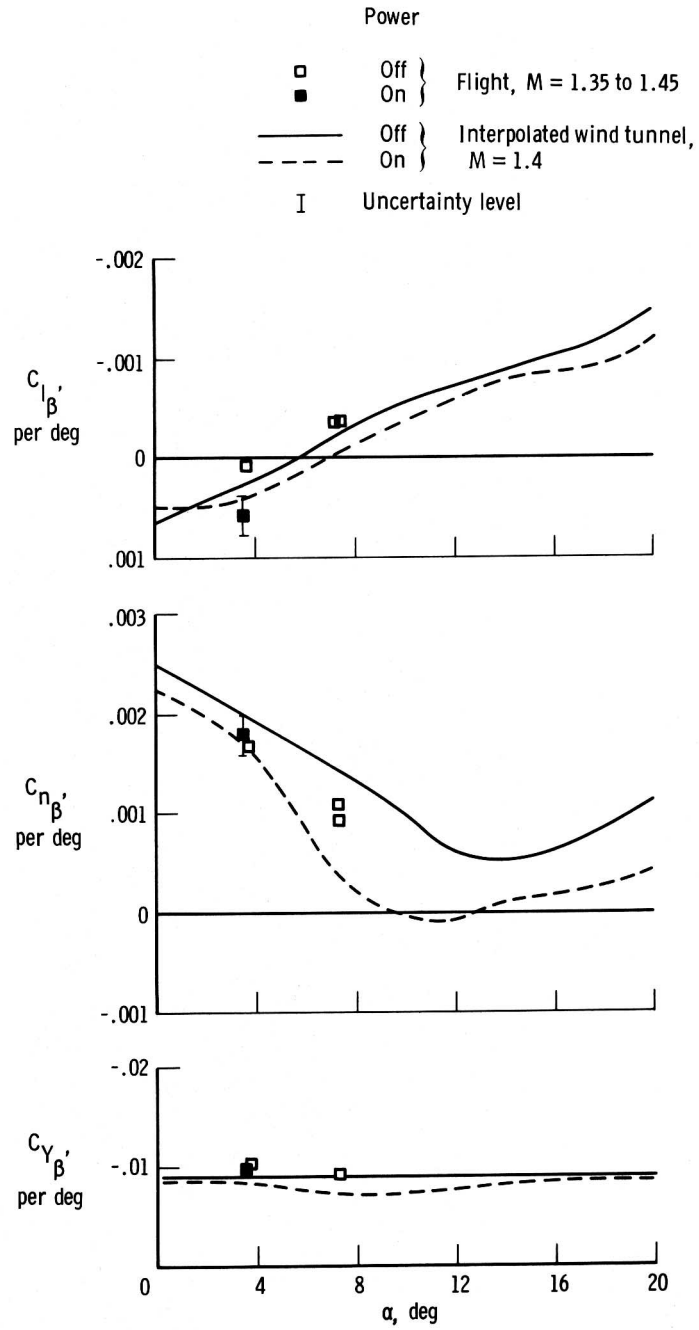
(d)  $C_{l_p}$ ,  $C_{n_p}$ ,  $C_{l_r}$ ,  $C_{n_r}$ .

Figure 14. Concluded.



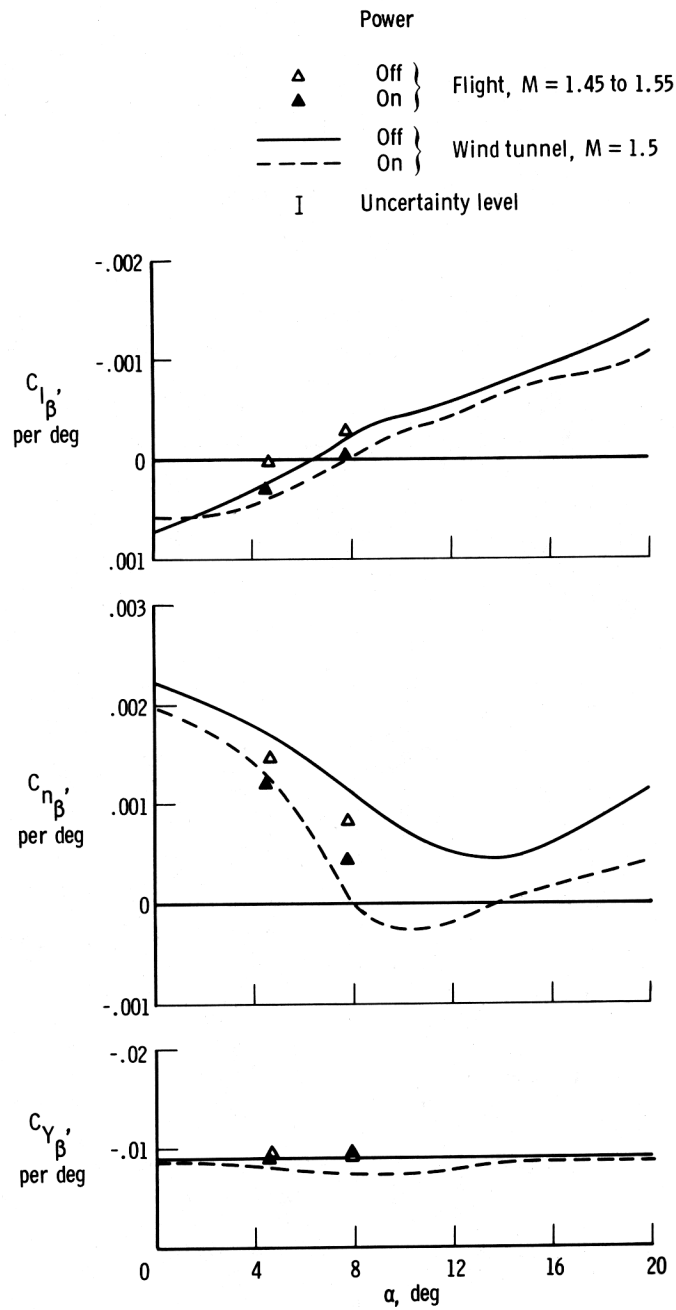
(a)  $C_{l_\beta}$ ,  $C_{n_\beta}$ ,  $C_{Y_\beta}$ .

Figure 15. Comparison of lateral-directional derivatives obtained from flight data with wind-tunnel results.  $M = 1.25$  to  $1.55$ ; transonic configuration; center of gravity =  $0.65 \bar{c}$ .



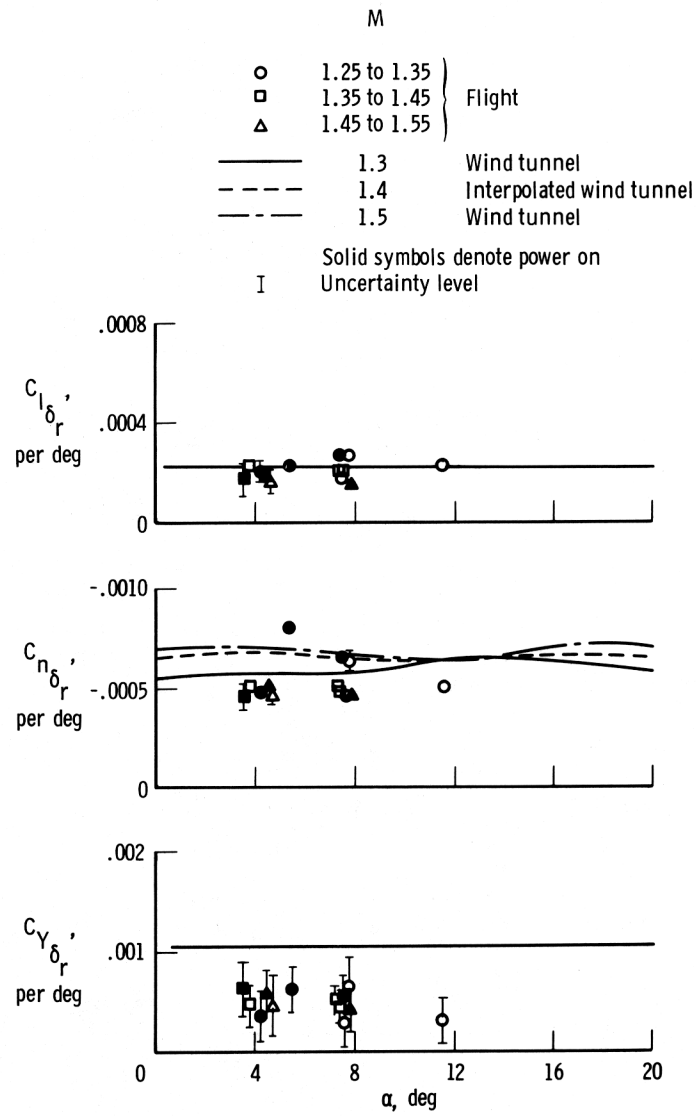
(a) Continued.

Figure 15. Continued.



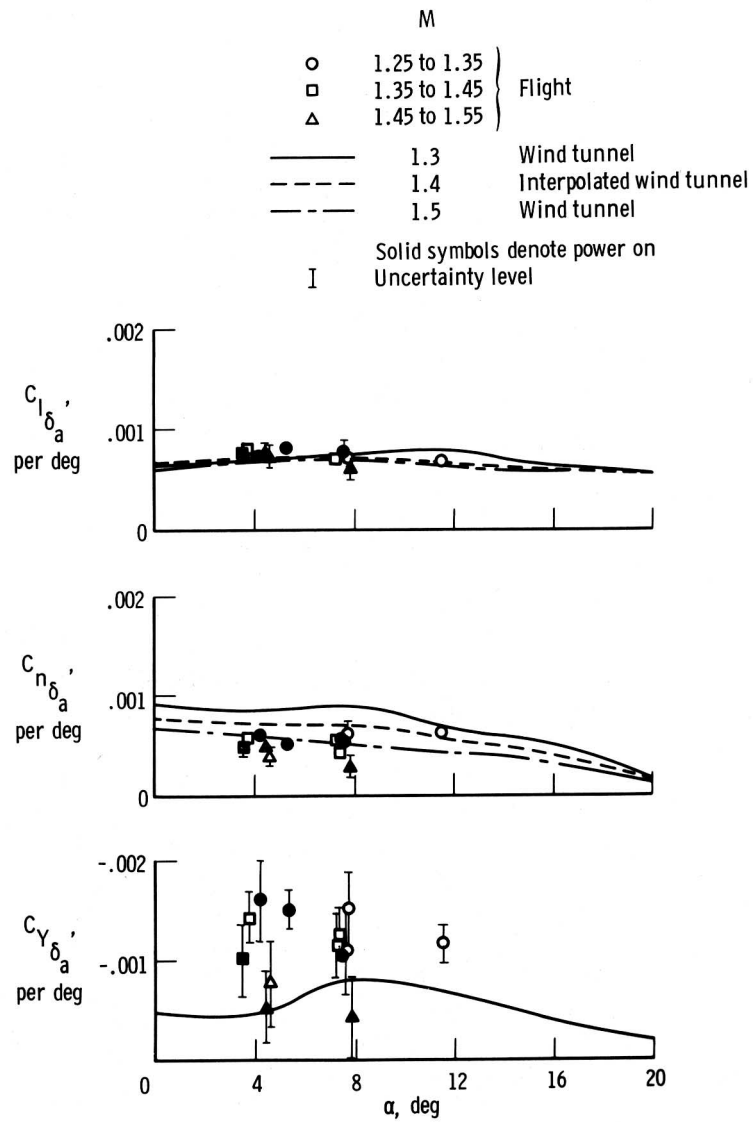
(a) Concluded.

Figure 15. Continued.



(b)  $C_{l_{\delta_r}}, C_{n_{\delta_r}}, C_{Y_{\delta_r}}$ .

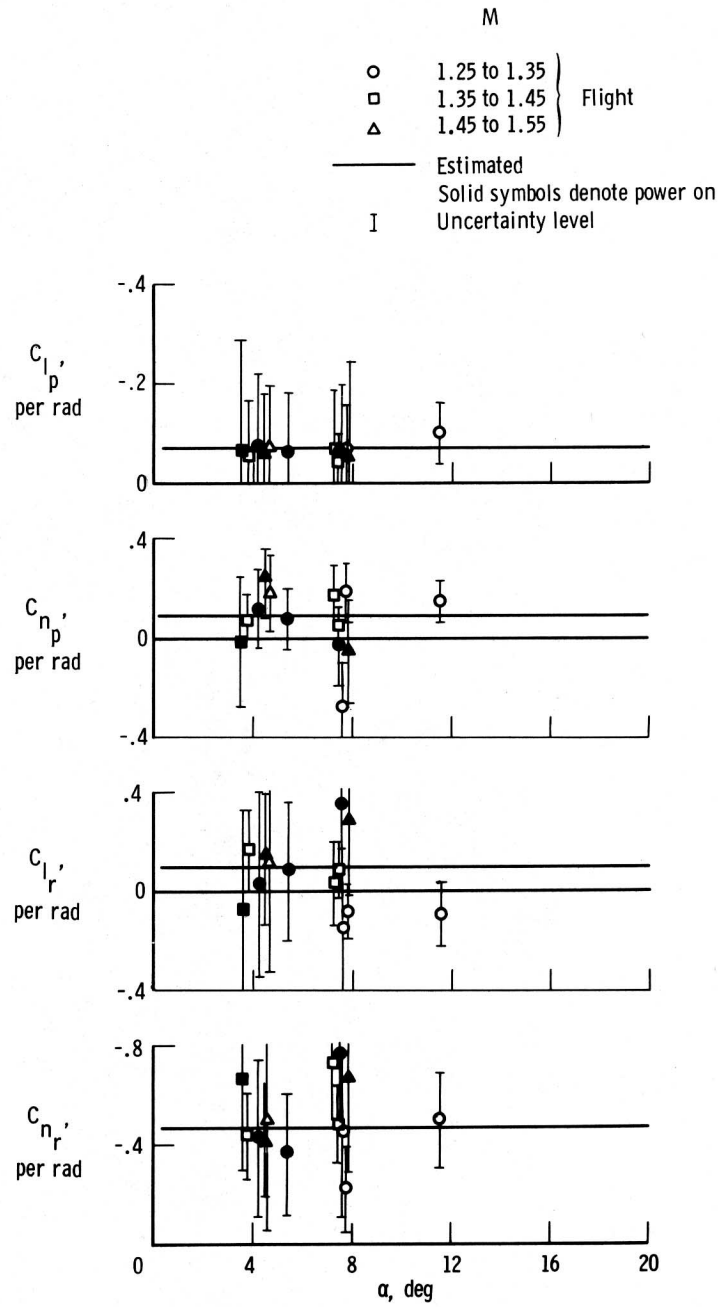
Figure 15. Continued.



(c)  $C_{l_{\delta_a}}$ ,  $C_{n_{\delta_a}}$ ,  $C_{Y_{\delta_a}}$ .

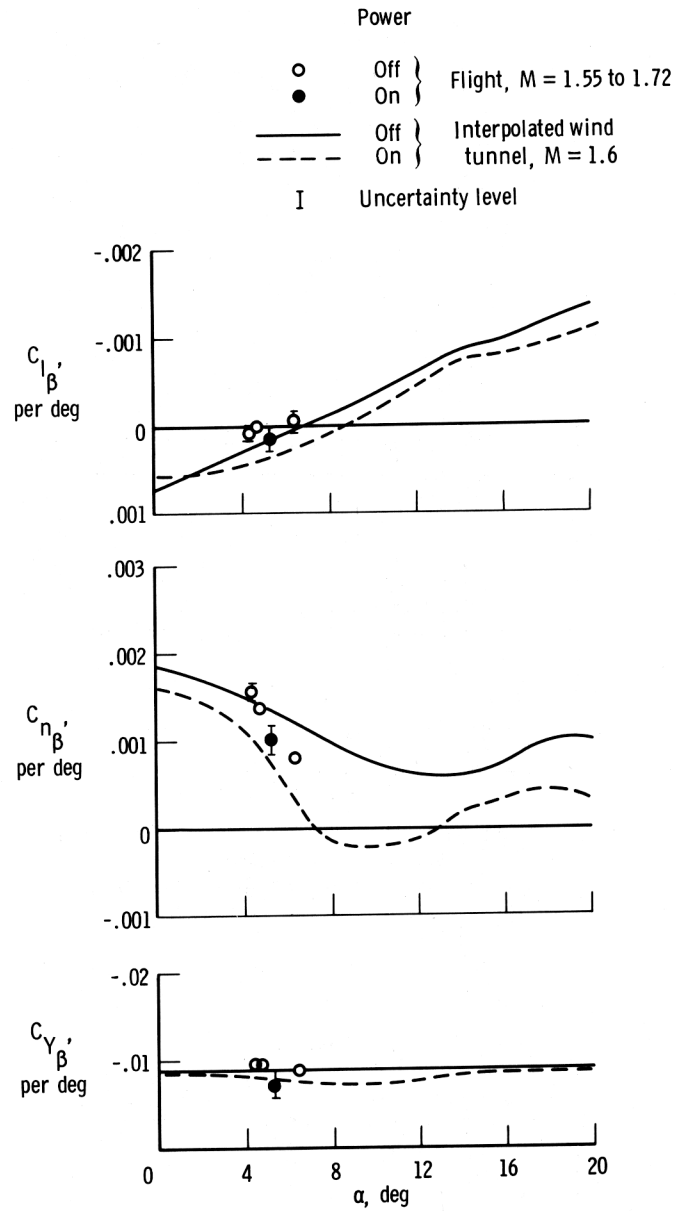
Figure 15. Continued.





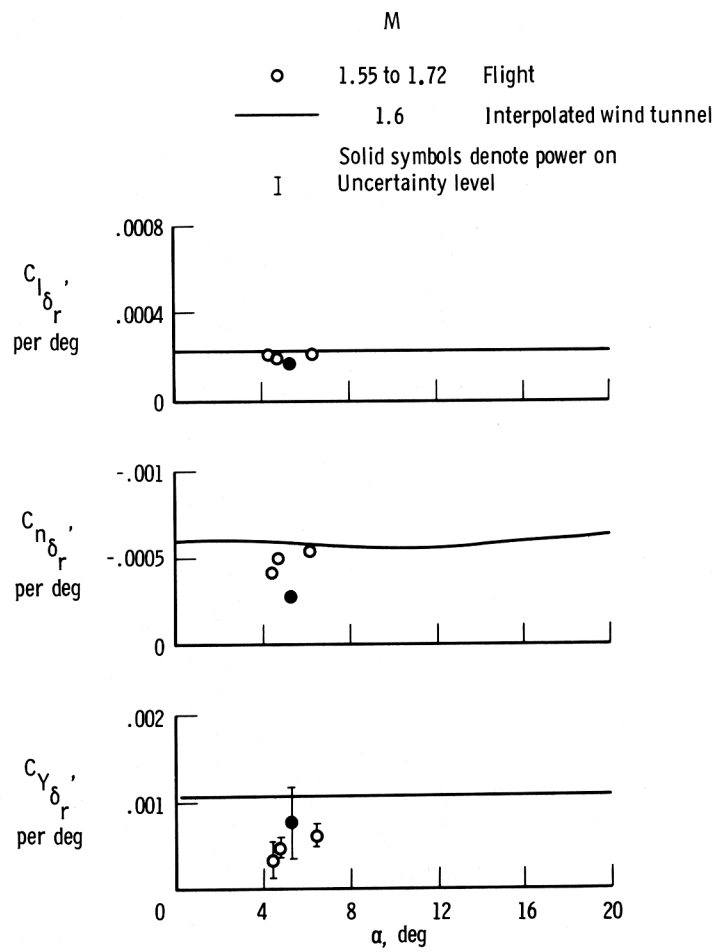
(d)  $C_{l_p}$ ,  $C_{n_p}$ ,  $C_{l_r}$ ,  $C_{n_r}$ .

Figure 15. Concluded.



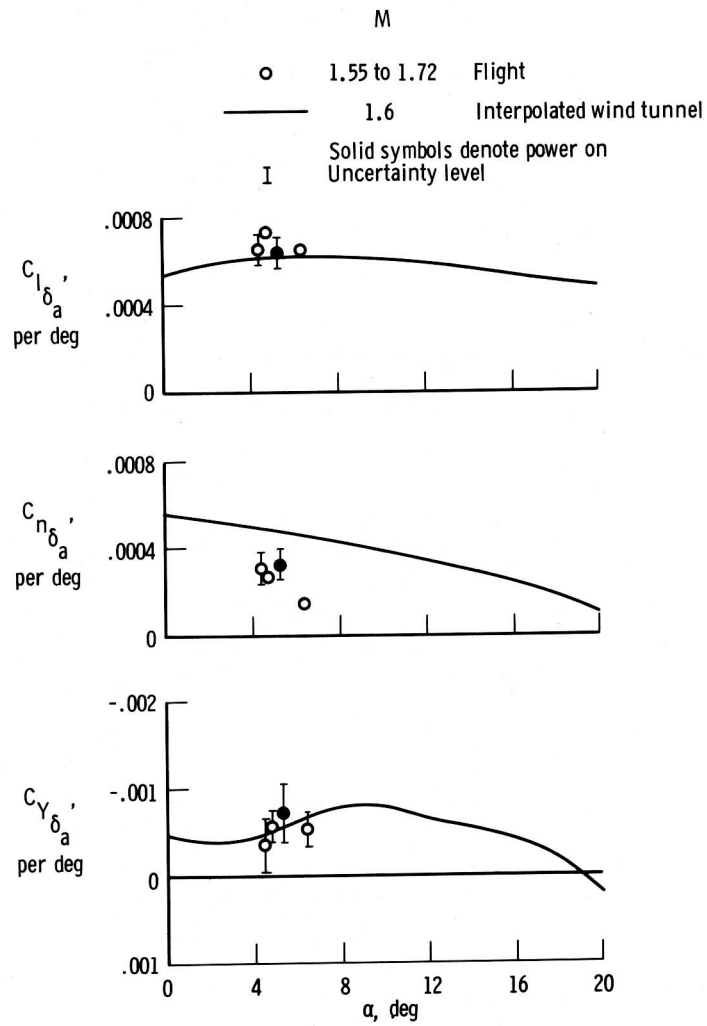
(a)  $C_{l_\beta}$ ,  $C_{n_\beta}$ ,  $C_{Y_\beta}$ .

Figure 16. Comparison of lateral-directional derivatives obtained from flight data with wind-tunnel results.  $M = 1.55$  to  $1.72$ ; transonic configuration; center of gravity =  $0.65 \bar{c}$ .



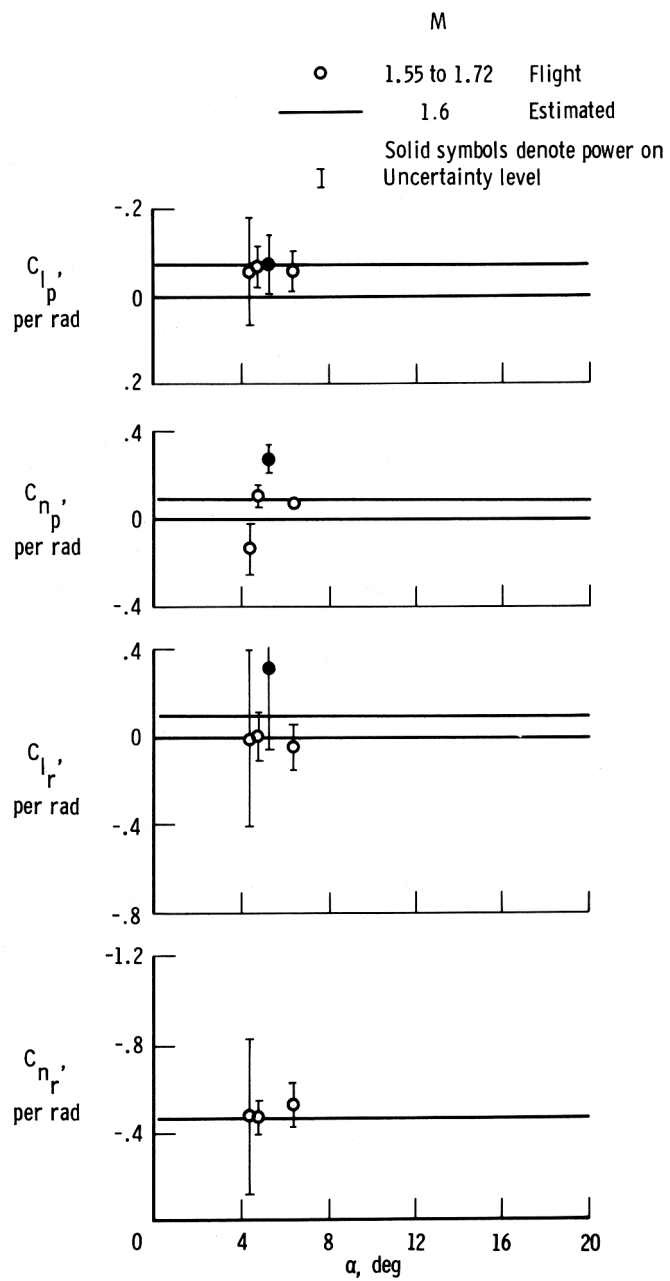
(b)  $C_{l_{\delta_r}}, C_{n_{\delta_r}}, C_{Y_{\delta_r}}$ .

Figure 16. Continued.



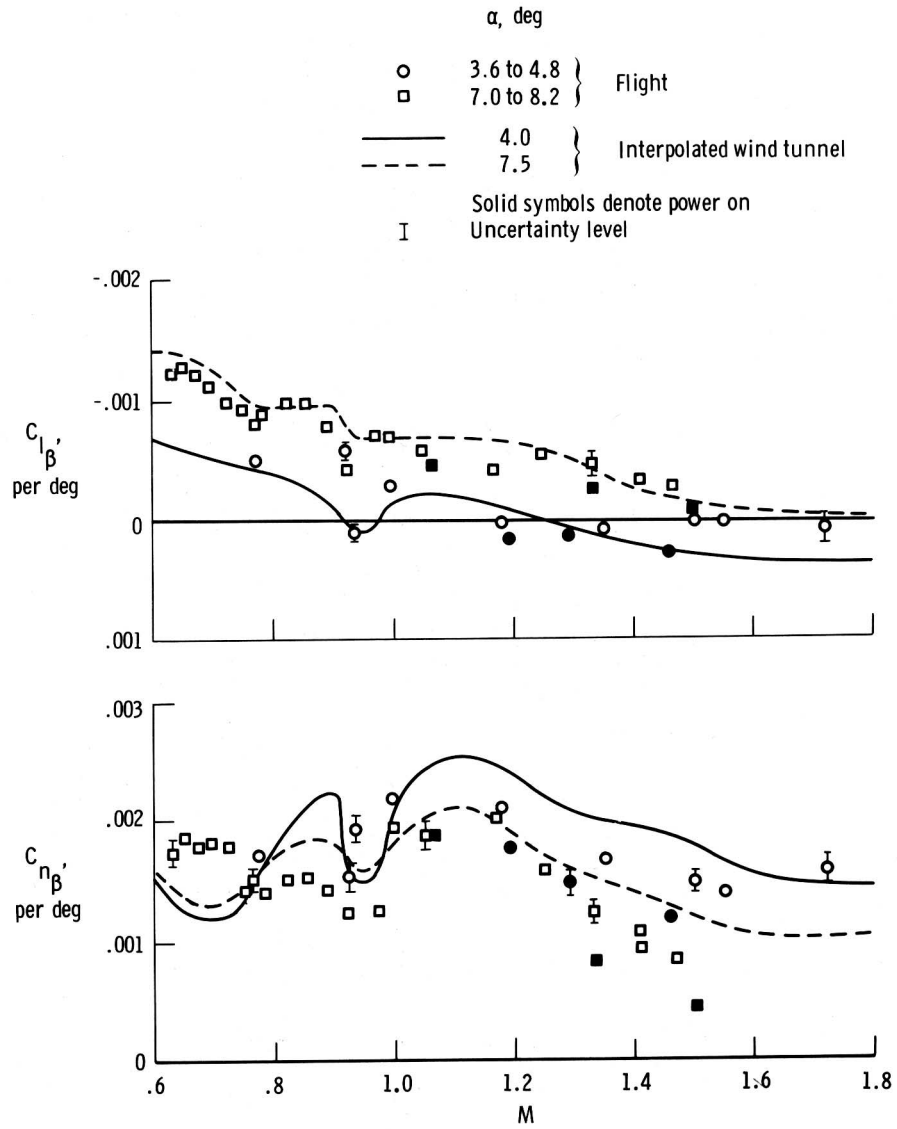
(c)  $C_{l_{\delta_a}}, C_{n_{\delta_a}}, C_{Y_{\delta_a}}$ .

Figure 16. Continued.



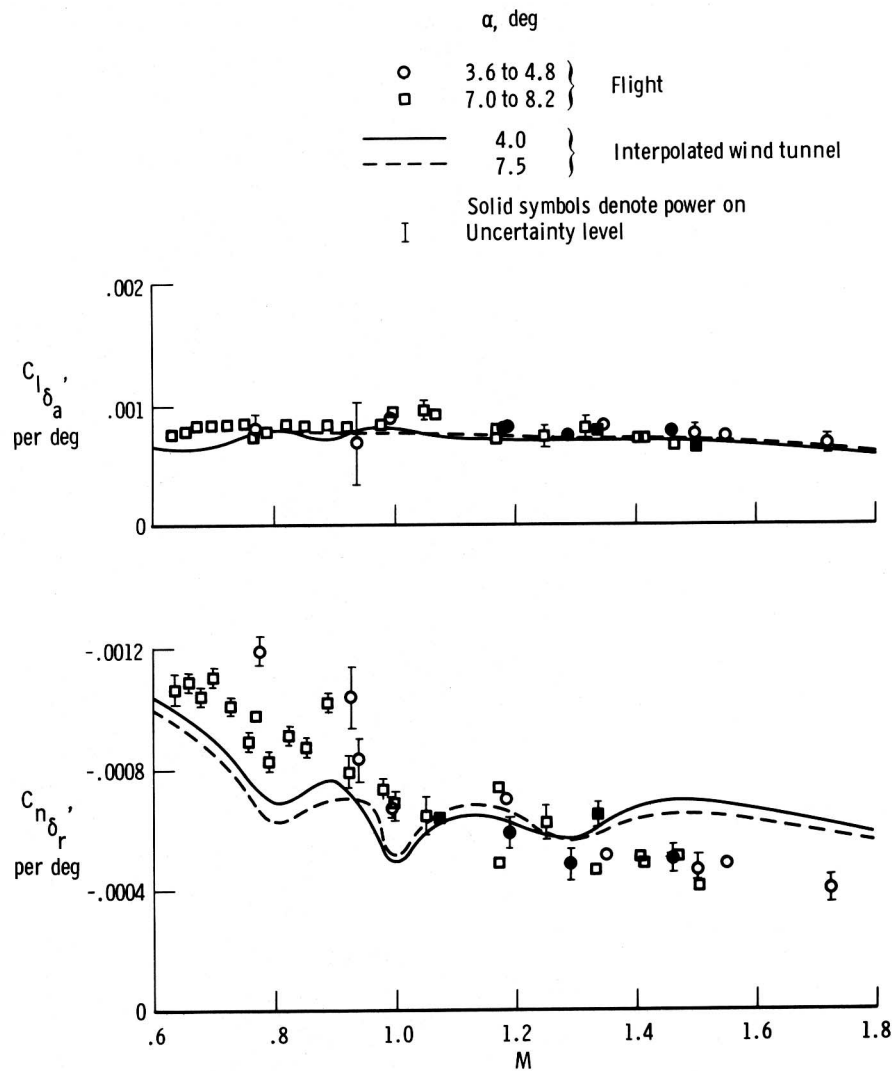
(d)  $C_{l_p}$ ,  $C_{n_p}$ ,  $C_{l_r}$ ,  $C_{n_r}$ .

Figure 16. Concluded.



(a)  $C_{l_\beta}$ ,  $C_{n_\beta}$ .

Figure 17. Comparison of lateral-directional derivatives obtained from flight data with wind-tunnel results for angles of attack near  $4^\circ$  and  $7.5^\circ$ . Transonic configuration; center of gravity =  $0.65\bar{c}$ .



(b)  $C_{l_{\delta_a}}, C_{n_{\delta_r}}$

Figure 17. Concluded.

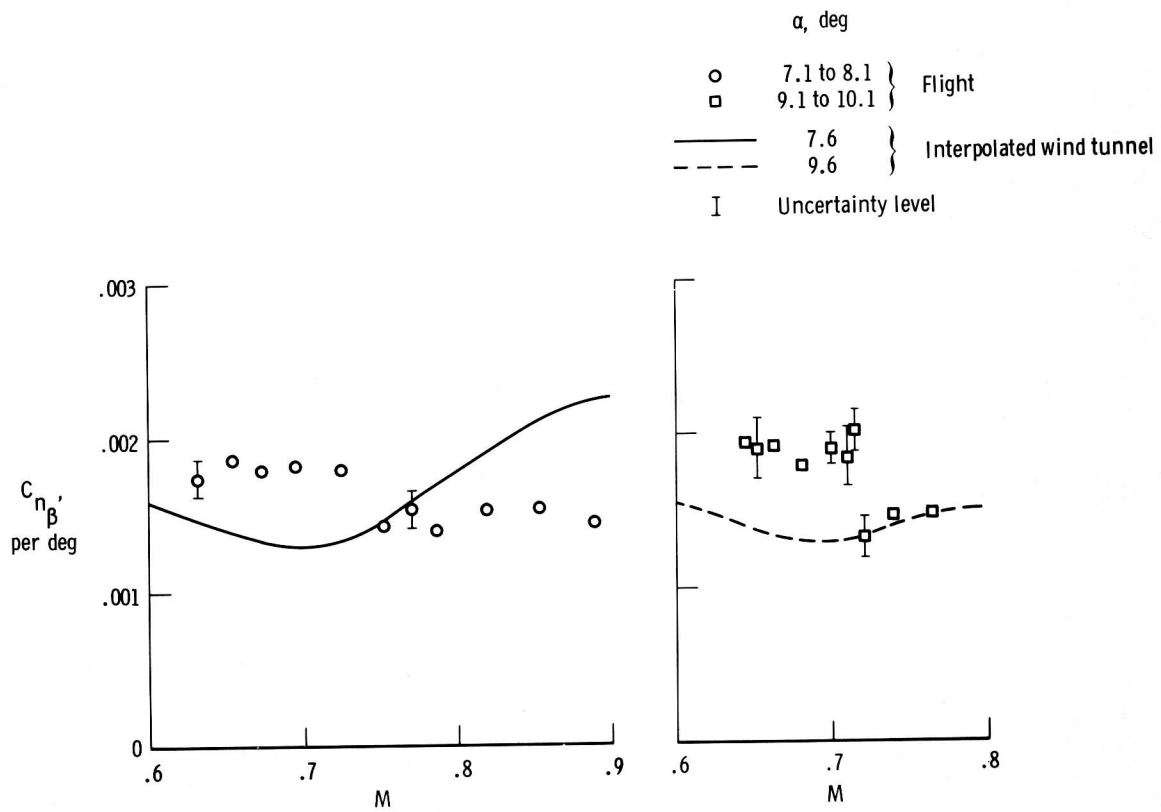


Figure 18. Comparison of  $C_{n_\beta}$  obtained from flight data with wind-tunnel results. Transonic configuration; center of gravity =  $0.65\bar{c}$ .



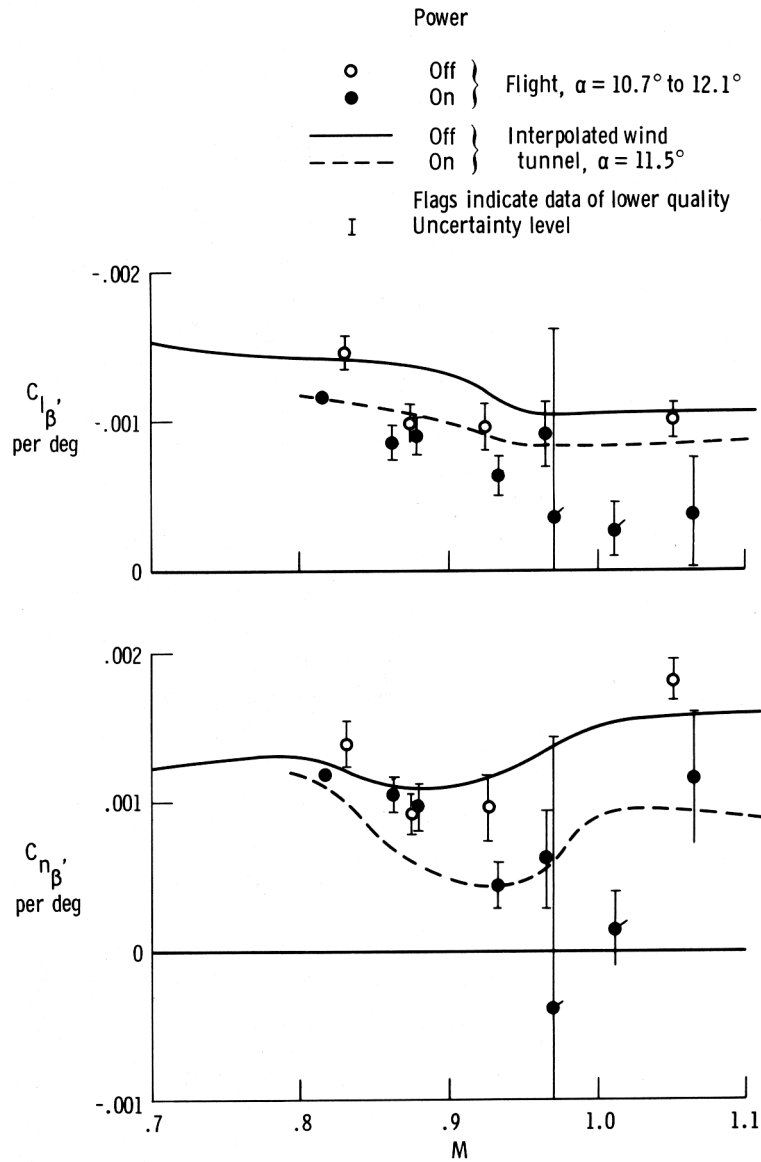


Figure 19. Comparison of  $C_{l_\beta}$  and  $C_{n_\beta}$  obtained from flight data with wind-tunnel results for angles of attack near  $11.5^\circ$ . Transonic configuration; center of gravity =  $0.65\bar{c}$ .

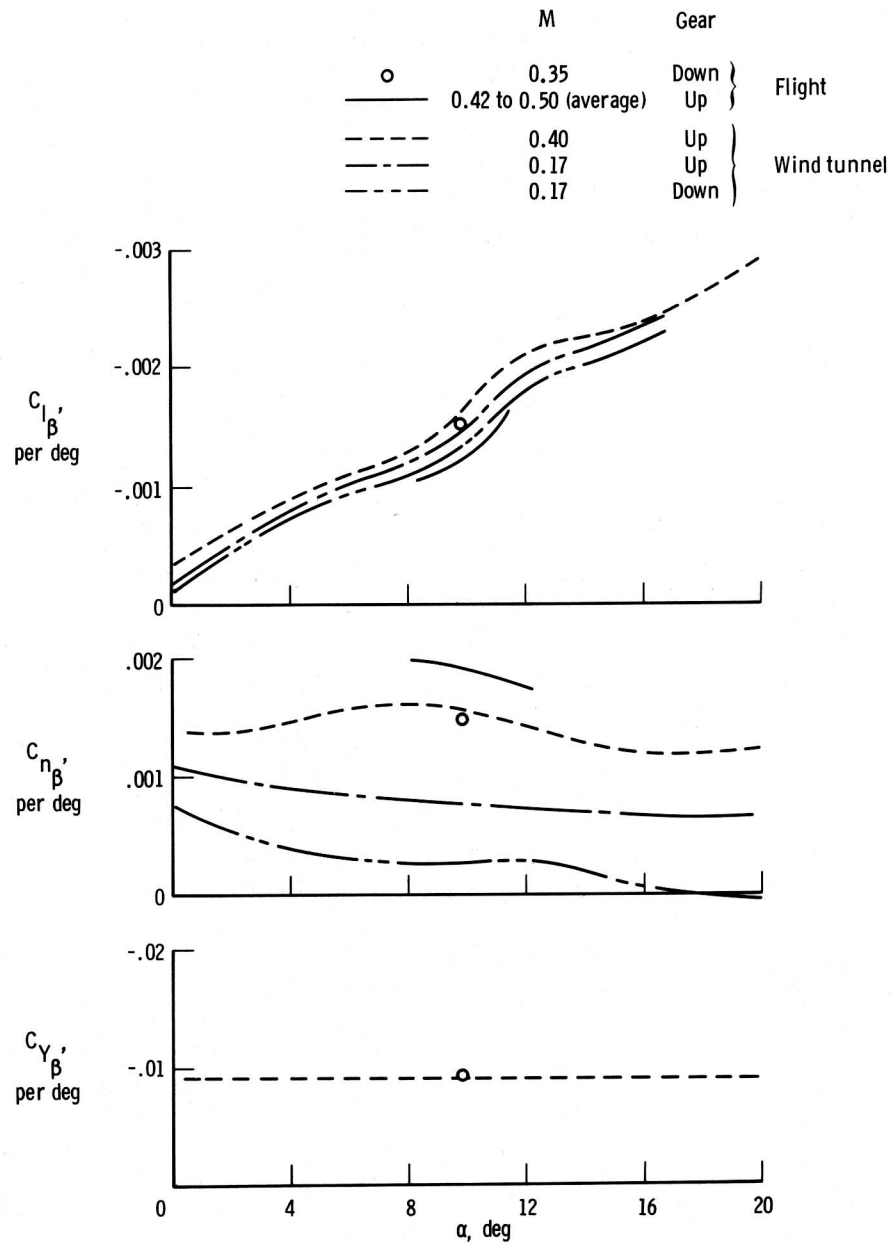


Figure 20. Effect of gear extension on lateral-directional derivatives obtained from flight and the wind tunnel. Subsonic configuration; center of gravity =  $0.65\bar{c}$ .

